Soft Matter

PAPER

View Article Online
View Journal | View Issue

Cite this: *Soft Matter*, 2025, **21**, 7289

Multifunctional poly(ionic liquid)/graphitic carbon nitride membranes: visible light-driven photodegradation coupled with antifouling properties

Hannah Schimke,[ab] Baris Kumru *[c] and Hanieh Bazyar *[b]

Received 30th April 2025,
Accepted 24th August 2025

DOI: 10.1039/d5sm00441a

rsc.li/soft-matter-journal

Polymer membranes are prime candidates for separation and purification processes, with their functionality enhanced by nanoparticle incorporation and diverse polymer structures. Poly(ionic liquids) (PILs), highly charged electrolyte-like polymers, are gaining interest as membrane polymer matrices. Embedding photocatalytic nanoparticles enables water purification through filtration and degradation reactions. Graphitic carbon nitride (g-CN), a metal-free semiconductor with visible-light activity, offers a promising approach for photoredox-based environmental remediation, though its powder form poses separation challenges. This work presents g-CN embedded PIL nanocomposite membranes fabricated *via* UV curing, characterized by structural, filtration, and surface properties. Photocatalytic performance and reusability under visible light are evaluated using methylene blue (model dye) and sulfadiazine (model antibiotic) under static conditions. A continuous filtration module with integrated light is developed to assess simultaneous filtration, degradation, and antifouling properties, demonstrating the membranes' potential for advanced water treatment.

1 Introduction

Access to clean water has been a major concern and among focus points of global sustainable development goals.[1] Microplastics, heavy metals, and organic micropollutants (MPs) such as dyes and antibiotics constitute serious threat by means of water quality.[2] While such impurities are hazardous to environment, their consumption must be omitted as they have high toxicity to human health. Dyes are among frequent MPs detected in wastewater.[3] For example, a large amount of methylene blue (MB) originates from textile industry, where high water consumption and the discharge of dyes into the aqueous environment are observed. Another MP from the group of antibiotics is sulfadiazine (SDZ), applied in human and veterinary medicine for the inhibition of bacterial infection.[4] For many decades, the antibiotic SDZ has been detected in wastewater treatment plants due to insufficient metabolism of the substance by living organisms, allowing antimicrobial resistance genes to evolve in the environment.

A promising approach for water purification is the use of membrane technology. Polymeric membranes are usually fabricated through casting methods.[5] The membrane is formed through phase inversion, using methods such as wet casting, dry casting, or thermally induced phase separation (TIPS).[6] Typical polymeric membranes fabricated using these methods are polytetrafluoroethylene (PTFE) and polyvinylidene fluoride (PVDF). These polymeric structures are utilized in low-pressure membrane systems, namely, microfiltration (MF) and ultrafiltration (UF).[7] Low-pressure membrane filtration is preferred for micropollutants removal, since unlike reverse osmosis and nanofiltration methods, it requires less energy and avoids producing a concentrated retentate that needs post-treatment.[8] Commercial polymeric membranes, however, have limitations due to membrane fouling and temperature sensitivity.[9] Increasing longevity of membrane technology is vital to improve the sustainability of environmental remediation. Polymers with advanced functionalities, such as ionicity and antifouling properties, are being explored as potential alternatives to conventional polymer materials to improve membranes' filtration performance.

Ionic liquids (ILs) are chemical substances attractive to many areas, *e.g.* in electrochemistry,[10] and renewable material extraction[11] to name a few. Ionic liquids possess favorable

[a] *Department of Process and Chemical Engineering, Hamburg University of Technology, Hamburg, Germany*
[b] *Transport phenomena, Chemical engineering Department, Faculty of applied sciences, Delft University of Technology, Van der Maasweg 9, 2629HZ Delft, The Netherlands. E-mail: h.bazyar@tudelft.nl*
[c] *Department of Aerospace Structures and Materials, Faculty of Aerospace Engineering, Delft University of Technology, Delft, The Netherlands. E-mail: b.kumru@tudelft.nl*

properties such as low volatility, non-flammability, high ionic conductivity, and high degree of chemical stability. Due to these benefits, ILs are known to be the benign alternatives to the volatile organic solvents.[12] Polymerizing ILs into highly ion-conductive polymer system has been recently implemented for membrane fabrication, as generation of controlled nanopores offer outstanding performances.[13,14] Poly(ionic liquid)s (PILs) are recognized by high surface charges and consisting of cations such as imidazolium, ammonium, and guanidinium in polymer backbone.[15] Among these, the vinylimidazolium-based PIL stands out as one of the most extensively synthesized and studied variants due to relatively straightforward radical polymerization of vinyl group. Cations within the PIL backbone are accompanied with different counter-anions such as Cl^-, $N(CF_3SO_2)^{2-}$, BF_4^-, PF_6^-, and ClO_4^-. The combination of hydrophilic and charged polymer chains renders them attractive for membrane and separation technologies.[16] Vinyl-derived PIL membranes are studied for gas separation, and alternatively as support material in heterogeneous catalysis.[17] Highly polar pores and the formation of hydration layers of PIL produce an attractive absorption sites for charged dyes in contaminated water.[18] Potential membrane studies on antifouling behavior due to charged structure indicate longevity of PIL based membranes in separation processes.[19]

Light induced wastewater treatment using semiconducting nanoparticles has been attracting interest in recent years, and commercial TiO_2-based systems provide efficient treatment.[20,21] Photoredox-generated charges create strong oxidizing species that degrade pollutants, with efficient charge separation being crucial for effective degradation.[22] However, due to its activation under UV light, the applications of the wide bandgap semiconductors like TiO_2 require high energy input.[23]

Graphitic carbon nitride (g-CN) is an emerging polymeric semiconductor that is active under visible light irradiation.[24] It can be synthesized from organic nitrogen-rich molecules (such as melamine) by thermal condensation, which affords highly aromatic metal-free photocatalytic structures.[25] g-CN is employed in a wide range of photocatalytic applications such as H_2 evolution,[26,27] CO_2 photoreduction,[28,29] and degradation of organic impurities.[30,31] While bare carbon nitride membranes prepared *via* vapor deposition offer outstanding performances on ion transport,[32–34] their limited-scale synthesis hinder water treatment applications where large quantities are demanded.

To overcome the separation issues associated with powder photocatalysts, g-CN is commonly integrated into polymer networks and membranes, creating reusable, easy-to-collect heterogeneous photocatalysts.[35] Several g-CN-based polymer composites have been reported for photocatalytic and environmental applications, highlighting the versatility of g-CN as a functional additive. For instance, g-CN has been integrated into polyacrylonitrile (PAN) to fabricate membranes for dye degradation and water purification. However, dispersion challenges and poor interfacial compatibility often limit performance.[36,37] Similarly, g-CN-polysulfone composites have been used to enhance photocatalytic activity and antifouling properties in ultrafiltration membranes,[38,39] while poly(vinylidene fluoride) (PVDF)/g-CN and mixed cellulose ester/g-CN systems have demonstrated improved separation efficiency under visible light.[40,41] Beyond traditional polymers, g-CN has also been combined with thermoplastic polyurethane to create flexible photocatalytic films for sewage treatment.[42]

While g-CN–polymer composites enable scalability for large-scale photocatalysis, a non-active polymer matrix can hinder charge separation, reducing photocatalytic efficiency.[43,44] Additionally, many of these systems suffer from limited multifunctionality or phase separation issues due to weak interactions between the polymer matrix and g-CN. Using a matrix that can take part in charge transfer process, such as poly(ionic liquid)s, photocatalytic activity can be improved compared to bare photocatalyst powder.[45] PIL matrix provides strong electrostatic and π–π interactions with g-CN, leading to homogeneous dispersion, enhanced mechanical stability, and the introduction of ionic conductivity and surface tunability. This synergistic combination enables the development of robust photocatalytically active membranes suitable for continuous operation in environmental remediation applications.

In this study, we investigate the combination of g-CN nanoparticles and PIL matrix to generate photocatalytic membranes through *in-situ* photopolymerization. Membranes are structurally analyzed in detail, and photocatalytic performance is assessed by removal of MB dye as well as SDZ antibiotic. Membranes' antibacterial and antifouling properties are further investigated. The performance of continuous filtration and simultaneous degradation is studied using a custom-made membrane filtration module with integrated light.

2 Materials and methods

2.1 Materials

Methylene Blue (dye content: ≥82%) and sulfadiazine (SDZ) (99.0%) are provided by Sigma-Aldrich, the Netherlands. 3-Ethyl-1-vinylimidazolium Bis(trifluoromethanesulfonyl)imide (>98.0%) and 3,3′-(butane-1,4-diyl)bis(1-vinyl-3-imidazolium)-bis(tri-fluoromethanesulfonyl)imide (>98.0%) are purchased from TCI EUROPE N.V., Belgium. Pentaerythritol tetrakis (3-mercaptopropionate) (>95%) and divinylbenzene (80%) are purchased from Sigma-Aldrich, the Netherlands. Graphitic carbon nitride (g-CN) is synthesized as reported in literature.[46] Ethylene glycol, used as the anti-solvent, is purchased from Boom B.V., Meppel, the Netherlands. The photoinitiator, phenylbis(2,4,6-trimethylbenzoyl) phosphine oxide (BAPO, 97%) with a maximum adsorption wavelength of 370 nm (MeOH), is purchased from Sigma-Aldrich, the Netherlands. Alginic acid sodium salt (SA) from brown algae, and $CaCl_2$ are provided by Sigma-Aldrich, the Netherlands.

2.2 Methodologies

2.2.1 Graphitic carbon nitride preparation. Graphitic carbon nitride (g-CN) is synthesized from melamine as reported in literature.[47] In short, the melamine precursor is placed in an aluminum crucible and thermally condensed in a nitrogen-

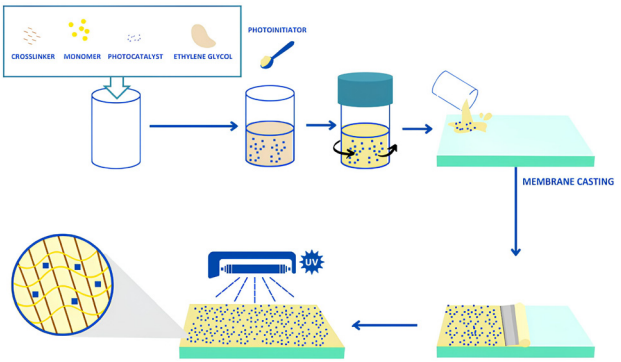

Fig. 1 Schematic illustration of the membrane fabrication process.

controlled oven at 550 °C. The surface morphology of g-CN nanoparticles is examined using scanning electron microscopy (JEOL JSM-6010LA, Japan). Micromeritics TriStar II Plus is used to measure the Brunauer–Emmett–Teller (BET) surface area. The optical properties of the materials are assessed in solid state using a UV-Vis spectrophotometer (Cary 500 Spectrophotometer, Agilent, United States) equipped with an integrating sphere in the range of 200–800 nm. The X-ray diffraction pattern of the g-CN is obtained using a Bruker D8 Advance X-ray diffractometer, *via* Cu Kα radiation.

2.2.2 Membrane fabrication method. Fig. 1 shows the schematic illustration of membrane fabrication procedure and Fig. 2 shows the chemical structures of the components used to fabricate the polymer membranes.

To fabricate the membranes, 1 g of monomer, 0.3 g crosslinker, 0.1 g ethylene glycol (dispersing agent for g-CN), and 5 mg g-CN powder are sonicated for 3 hours to form a fine dispersion, using continuous bath cooling to prevent undesired gelation. For reference membranes, g-CN is omitted. After sonication, 0.3 g photoinitiator is added, and the mixture is further sonicated for 5 minutes before casting and photopolymerization.

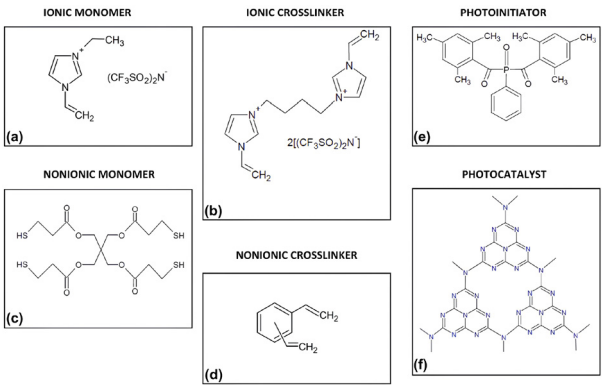

Fig. 2 Chemical structures of the different components for the fabrication of the ionic and non- ionic membranes: (a) 3-ethyl-1-vinylimidazolium bis(trifluoromethanesulfonyl)imide, (b) 3,3′-(butane-1,4-diyl)bis (1-vinyl-3-imidazolium) bis(trifluoromethanesulfonyl)imide, (c) pentaerythritol tetrakis(3-mercaptopropionate), (d) divinylbenzene, (e) phenylbis(2,4,6-trimethylbenzoyl) phosphine oxide, (f) graphitic carbon nitride (g-CN) depiction in 2D.

A common doctor blade casting process is used to fabricate membranes. The casting knife, with adjusted thickness, is used to spread the polymer solution evenly over the casting glass plate, which is pre-cleaned using acetone. The prepared wet film is placed under the UV irradiation to initiate the polymerization. A dimmable custom-built UV chamber is built using a light-emitting diode (LED) light source (Powerstar Series) and a heat sink, which are purchased from from RS Components B.V., the Netherlands. The UV LED with a maximum power of 1200 mW and a wavelength of 370 nm is used to excite the photoinitiator. To achieve full polymerization, the duration is set to 120 min. After the polymerization process, the polymerized membrane is detached from the glass surface by either wetting the membrane top surface or immersing the plate in the deionized water. A digital micrometer (Mitutoyo, MDC-25PX) is used to measure membrane thickness on dry membrane samples on at least 5 locations. The membranes are stored in water until further analysis.

The PIL/g-CN composite membrane is fabricated *via in-situ* photopolymerization. Electrostatic cross-linking within PIL and nonsolvent complexation initiated by UV exposure are crucial for developing the porous architecture and increasing the surface area.

Reference non-ionic hydrophobic membranes are further prepared to assess the influence of ionic surface and hydrophilicity on membrane-based photodegradation. As g-CN exhibits blue fluorescence under UV light,[48] g-CN embedded polymer composites (PIL/g-CN membranes) possess similar behavior (See SI, Fig. S1 for the picture of the membrane under UV light).

2.2.3 Surface morphology. The surface morphology of membranes is investigated using scanning electron microcopy (SEM) (JEOL, JSM-6010LA, Japan). The stored membranes in water are freeze-dried overnight to remove moisture. This process involves vacuum-induced sublimation which enables retention of porous structure for imaging. After freeze-drying, membranes are sealed to prevent moisture absorption during storage. The freeze-dried sample is then cut to size and affixed to a sample holder with double-sided adhesive tape. For top and bottom surface imaging, separate samples are prepared. Cross-sectional analysis involves breaking the sample using liquid nitrogen. Each sample undergoes gold coating using a sputter coater for 30 seconds at 20 mA. SEM parameters are optimized in JEOL InTouchScope™ software, with consistent magnifications for comparable images. This process aids in visual determination of pore size and membrane structure.

2.2.4 Contact angle measurements. Membranes' water contact angle values are measured using contact angle goniometer (OCA25, Dataphysics, Germany). Samples of 1 × 1 cm^2 are mounted on glass slides using double-sided adhesive tape.

Static water contact angle is measured using a 2 μL water drop (Milli-Q grade), dispensed using a micro syringe dosing system. This measurement is performed at least on 6 different spots on each sample. The static contact angles values are

recorded after 10–15 s to allow for stabilization. If rapid absorption occurred (indicating complete wetting), captive bubble technique is used, in which membrane sample is immersed in water and contact angle of air is measured by dispensing 6 μL droplet of air.

Dynamic contact angle is measured *via* the advancing/receding contact angle (ARCA) measurement. In the ARCA setting, the initial droplet volume is increased to 6 μL at the rate of 0.5 μL s^{-1} for at least 7 cycles. The advancing and receding contact angles are measured as the droplet size is altered by adding or withdrawing water within 6 s, with a 2 s pause in between. All contact angle measurements are repeated at least 2 times and averaged for consistency.

2.2.5 Pure water permeability. The pure water permeability of membranes is measured from permeating water flux through the membrane per unit area/time/transmembrane pressure (TMP) in dead-end filtration mode. It is obtained using the POROLUX™ Revo with a gas–liquid extension purchased from APTCO TECHNOLOGIES NV, Belgium. The schematic illustration of the set-up is shown in Fig. 3.

2.2.6 Pore size distribution. A gas–liquid porometer ((POROLUX™ Revo, APTCO TECHNOLOGIES NV, Belgium) is used to obtain the membranes' pore size and pore size distribution. The standard procedure involves membrane wetting using a low surface tension wetting liquid (Porefil™, wetting liquid for porometers, fluorinated hydrocarbon, Porometer, Belgium) before measurement. However, direct wetting is ineffective since membranes are stored in water and the pores are pre-filled with water. The membrane samples are thus freeze-dried overnight, ensuring open pores, followed by immersion in Porefil for 1 h prior to the measurement. This method allows for effective wetting without causing swelling, critical for precise pore size evaluation. Nitrogen gas is then pushed through the membrane at different pressure values leading the displacement of the wetting liquid. The corresponding gas flow rate is measured simultaneously (see SI, section "Gas–liquid poromtery-Pore size distribution" for more details on the experimental procedure, flow *vs.* pressure plot (Fig. S2), and pore size distribution of all fabricated membranes (Fig. S3 and S4)).

2.2.7 Swelling ratio. The membrane samples (3 × 3 cm^2) are weighed dry and then immersed in water for 24 h. Excess water is removed and the samples are weighed again to calculate the swelling ratio. This process is repeated three times for each membrane type. The swelling ratio (SR) of the membranes (%) is calculated using

$$\mathrm{SR} = \frac{W_{\mathrm{wet}} - W_{\mathrm{dry}}}{W_{\mathrm{dry}}} \times 100, \quad (1)$$

where W_{wet} and W_{dry} are the weight of the wet and dry membranes (g), respectively.

2.2.8 Dye adsorption experiments. To study the photoactivity of the composite PIL/g-CN membranes, including the adsorption and degradation behavior, adsorption experiments is performed by immersing membrane with a known weight into the methylene blue (MB) solution in darkness as described below.

0.25 g membrane samples are subjected to 3 mg L^{-1} MB containing water for 2 h in the dark to reach adsorption–desorption equilibrium. Following the completion of the adsorption period, the catalytic reaction commences using visible LEDs (100 W, 8510 Lm, 6000 K daylight white, 220–240 V, Spectrum, LCB LED EUROPE B.V., the Netherlands). The reaction chamber, lined with an aluminum foil, is shined using these visible LED lamps. The adsorption duration is determined to be 2 h. After 2 h in dark, the MB degradation is started by light irradiation. The degradation rate is determined by taking samples of the dye solution at 30-minute intervals. Fig. 4 shows the schematic illustration of the set-up used for dye adsorption experiments of the membranes.

The amount of the adsorbed MB or adsorption capacity at equilibrium (q_e (mg g^{-1})) is determined using the mass balance equation

$$q_e = \frac{(C_0 - C_e) \times V}{m}, \quad (2)$$

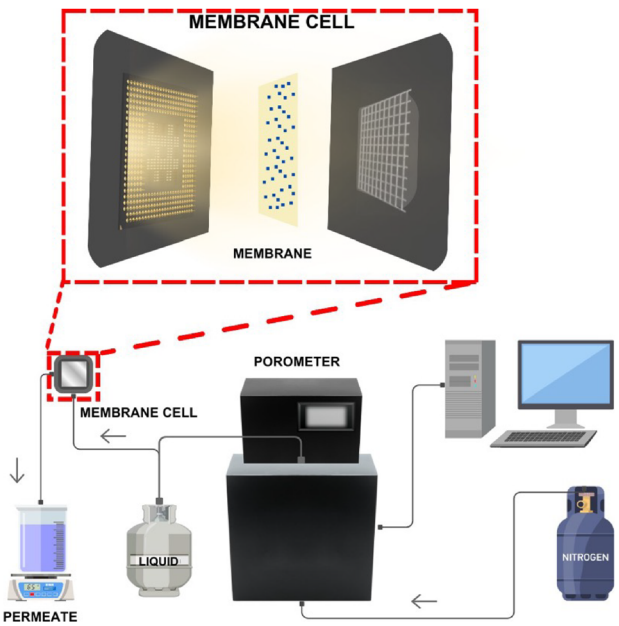

Fig. 3 Schematic illustration of the experimental set-up for measuring pure water permeability in dead-end configuration along with the customized membrane cell.

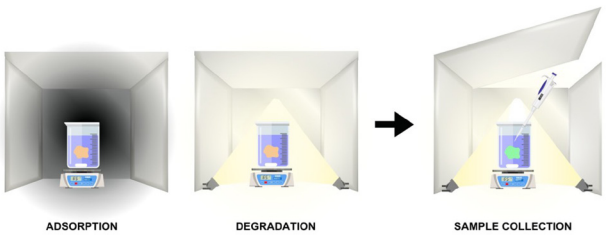

Fig. 4 Schematic illustration of the experimental set-up used to study the dye adsorption properties of the membranes.

where C_0 and C_e (mg L^{-1}) represent the initial and equilibrium concentrations of MB, respectively, V (mL) is the initial volume of the solution and m (g) is the mass of the membrane adsorbent.

2.2.9 Photocatalytic degradation experiments. The photocatalytic degradation experiments are performed in a two-step process as described below.

Step 1: Preliminary assessment of photocatalytic performance

The initial phase focused on evaluating the membranes' ability to degrade pollutants under visible light. Similar experimental procedure and set-up as those used for the dye adsorption experiments (see section ''Dye adsorption experiments''), are used in this step. Two model contaminants, namely methylene blue (MB), a common dye, and sulfadiazine (SDZ), an antibiotic, are studied.

It is worth noting that before assessing the membranes' ability to degrade SDZ, photocatalytic activity of pure g-CN powder is first evaluated. Further details of the experiments for MB and SDZ can be found in the SI, section ''Photocatalytic degradation experiments''.

Step 2: Simultaneous adsorption and degradation in filtration Mode

The photocatalytic degradation and antifouling properties of membranes are carried out in dead-end filtration configuration using similar set-up for pure water permeability experiments (Fig. 3). For simultaneous photodegradation and removal of the micropollutants, a custom-built membrane module featuring the light source is designed and fabricated in cooperation with the electronic and mechanical support division (DEMO) at the TU Delft, the Netherlands. The LED components are mounted into a printed circuit board (PCB). The module comes with two LED PCBs, one for UV and one for visible light (UV wavelength: 370 nm), which serve as the light source activating carbon nitride photocatalyst in composite membranes. The schematic illustration of the membrane module is shown in the zoomed-in image of Fig. 3.

Methylene Blue (MB). The UV-Vis spectrophotometer (DR6000, Hach, Germany) is utilized to determine the MB concentration. The required polyethylene cuvettes for the UV measurements are supplied by SARSTEDT AG & Co. KG. For the UV-Vis calibration method a single wavelength is chosen (see the experimental procedure for MB in step 1).

Sulfadiazine (SDZ). For more realistic water treatment simulation, a 20 mg L^{-1} SDZ solution is prepared and introduced into the custom membrane filtration cell equipped with an integrated visible light source. The system is operated under dead-end filtration, and samples are collected from the permeate for analysis.

SDZ concentrations are determined using high-performance liquid chromatography (HPLC) (SHIMADZU, Japan) equipped with a C18 column, purchased from Phenomenex, CA, United States (Kinetex 2.6u C18 100 A). The identity and purity of SDZ is further confirmed by proton nuclear magnetic resonance (^{1}H-NMR) spectroscopy (Bruker, USA). Samples are filtered through a 0.2 μm syringe filter, transferred into HPLC vials, and stored at 4 °C for subsequent analysis.

The initial concentration of MB and SDZ (C_0) is determined using a calibration curve, which relates absorbance to known concentrations of the dye (see SI, Fig. S10 and S13 for calibration curves of MB, and SDZ, respectively). The removal of the micropollutant by the membrane is given by

$$R(\%) = \frac{(C_t - C_e)}{C_t} \times 100, \quad (3)$$

where C_t and C_e refer respectively to the initial and equilibrium (final) concentration of the adsorbate after treatment, and R is the percentage removal.

2.2.10 Antifouling experiments. The antifouling performance of PIL membranes are compared with that of commercial PTFE membranes by filtering a sodium alginate (SA) solution in the presence of $CaCl_2$ in dead-end filtration mode (see Fig. 3). Two different SA solutions with concentrations of 5 mg L^{-1} and 10 mg L^{-1} are prepared to study the influence of the foulant concentration on the membranes' antifouling performance. The selection of these concentrations is based on real concentrations found in the seawater.[49]

The SA solution is prepared in two ways to form (i) an alginate layer and (ii) alginate beads on the membrane surface during the filtration process. (i) To form the alginate layer, two solutions are prepared simultaneously: 1.68 g of $CaCl_2$ in 500 mL of water, and 5 mg (or 10 mg) of SA in 500 mL of water, each stirred for 2 h. These solutions are then combined and immediately used for the filtration experiment. (ii) To produce alginate beads, 1.68 g of $CaCl_2$ is initially dissolved in 1 L of Milli-Q water, ensuring thorough dissolution. Subsequently, 5 mg (or 10 mg) of SA is introduced into the solution while stirring vigorously to achieve uniform distribution. This mixture is then left to stir for a 24 h at room temperature, allowing for the formation of alginate beads through controlled chemical interactions.

Filtration is conducted at an applied pressure of 0.1 bar for 1 h, utilizing an effective membrane surface area of 6.25×10^{-4} m^2. The permeate from each membrane and each sodium alginate concentration is collected in an Erlenmeyer flask placed on a precision balance.

The permeating flux J (m^3 m^{-2} s^{-1}) through the membranes is calculated using,

$$J = \frac{V}{A \cdot t} \quad (4)$$

where V is the volume of the collected permeate (m^3), A is the effective membrane area (m^2), and t is the filtration time (s). After filtration experiments, the membranes are examined using SEM imaging. To analyze the content of the SA, samples of both the feed and the permeate are collected and tested using a UV-VIS spectrophotometer at a wavelength of 200 nm.

2.3 Results and discussions

2.3.1 Graphitic carbon nitride characterization. UV-Vis spectra of g-CN confirms light adsorption in the range of

Table 1 Membrane thickness and swelling ratio (SR) of the investigated membranes (values after ± shows the standard deviation from 5 measurements)

Membranes	PIL polymer	PIL[a]	PIL[a]/ g-CN	Nonionic polymer	Nonionic/ g-CN
Thickness [μm]	91 ± 7	97 ± 5	90 ± 8	110 ± 7	113 ± 5
SR [%]	92	62	42	25	15

[a] Contains ethylene glycol as the antisolvent.

260–380 nm, and XRD profile exhibits typical (100) and (002) peaks, indicating sheet-like structure (see SI, Fig. S5(a) and (b)). The SEM shows no special morphology, which is as expected since no templating nor additives are used during synthesis (see SI, Fig. S5(c)).

2.3.2 Membrane swelling ratio and pore size distribution. Table 1 summarizes the swelling and thickness of PIL and nonionic membranes with and without g-CN. The pictures of these membranes are shown in the SI, Fig. S6. PIL matrix polymers demonstrated the highest swelling ratio at (92%), attributed to their inherent hydrophilic properties. Including g-CN into the membrane matrix reduces membrane swelling by additional crosslinking of polymerized matrix.[50] Addition of an antisolvent, like ethylene glycol, also reduces swelling, and PIL membranes containing ethylene glycol shows a swelling ratio of 62%. Reference samples based on more hydrophobic polymers compared to PIL matrix have much lower swelling ratios as expected.

FTIR analysis is performed on the prepared membranes (ionic and nonionic) and the results are shown in the SI, Fig. S7. While a clear structural difference between PIL matrix and reference matrix is visible by means of distinct peaks (S═O in PIL, C═O in nonionic, C═N in PIL, *etc.*), addition of carbon nitride is not detectable for the case of PIL as they possess similar functional groups. g-CN incorporation is visible in nonionic matrix membranes as peaks of triazine rings arising from g-CN is detectable around 890 cm^{-1}.

SEM images of the top, bottom, and cross section of the fabricated PIL/g-CN membranes are shown in Fig. 5. The SEM images of the nonionic counterpart as well as the ionic and nonionic polymer matrices are illustrated in the SI, Fig. S8. The membrane top surface (Fig. 5a) reveals the presence of pores with a pore size smaller than 10 μm in diameter, indicating a characteristic of microfiltration membranes. The pores are controlled by the amount of antisolvent, which is 6 wt% of ethylene glycol. As the amount of g-CN of 0.3 wt% is relatively small, it is not detectable in the SEM images.

The presence of g-CN nanoparticles may result in additional roughness and surface area, potentially affecting the permeability and selectivity of the membrane. SEM images of the cross section (Fig. 5c) indicate a homogeneous distribution of pores, measuring around 1 μm in pore diameter. The pores appear evenly and symmetrically round, and a regular pore size pattern is visible. Using ethylene glycol as the antisolvent, generates high but irregular porosity (see SI, Fig. S9). In this

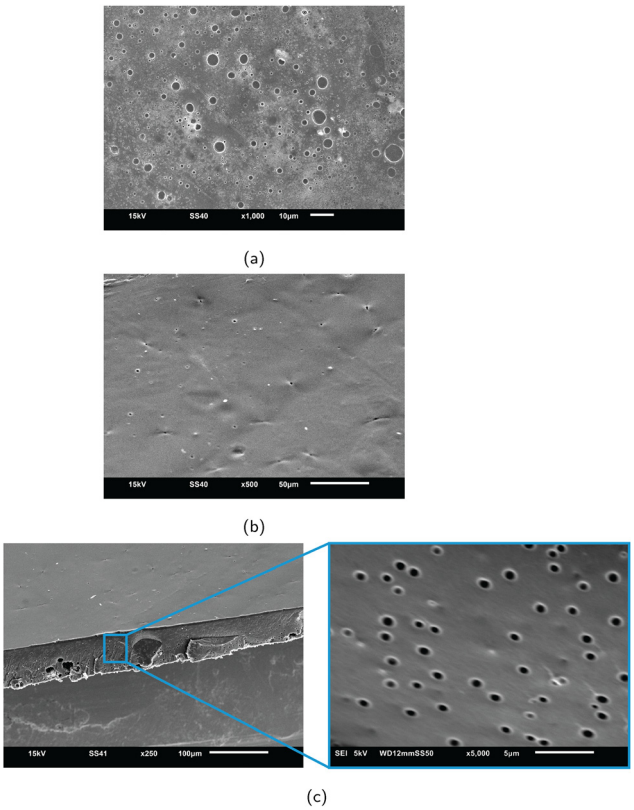

Fig. 5 SEM images of composite PIL/g-CN membranes: (a) top, (b) bottom, and (c) cross section.

case ethylene glycol acts as porogen by not reacting in the matrix. The images depict these pores as consistently round and symmetrically shaped, forming a regular pattern throughout the membrane structure.

This homogeneity in pore distribution is critical for ensuring predictable and efficient filtration performance. To further characterize the membrane's through pore size, the pore size distribution is measured using the gas–liquid porometery (see Materials and methods, section "Pore size distribution" for the details of the experiment). This analysis, as summarized in Table 2, focused on determining the range and consistency of through-pores across each membrane sample. The mean pore size is an average measure of the pore size within the membrane. The PIL membrane has a mean pore size of 0.90 ± 0.002 μm, while the PIL/g-CN composite membrane has a larger mean pore size of 1.37 ± 0.02 μm. The nonionic polymer membrane and the nonionic/g-CN composite membrane also have mean pore sizes of 1.00 ± 0.12 μm and 1.37 ± 0.02 μm, respectively. The corresponding flow *vs.* pressure plot for composite PIL/g-CN membranes along with the pore diameter plot for various membranes are shown in the SI, Fig. S2 and S3.

The pore size distribution curve of the membranes are further shown in the SI, Fig. S4. As shown in Fig. S4(a), the PIL/g-CN has a broader pore size distribution curve covering a wider pore size range than that of the PIL membrane. This is

Table 2 Pore size distribution parameters for the investigated ionic and nonionic membranes, measured *via* gas–liquid poromtery using a membrane area of 298.6 mm^2

Membranes	PIL polymer	PIL/g-CN	Nonionic polymer	Nonionic/g-CN
Smallest pore [μm]	0.29 ± 0.05	0.4 8 ± 0.15	0.33 ± 0.07	0.3180 ± 0.0001
Mean pore size [μm]	0.90 ± 0.002	1.37 ± 0.02	1.0 ± 0.12	1.37 ± 0.02
Max pore size [μm]	8.41 ± 0.03	12.62 ± 0.01	9.25 ± 1.22	12.63 ± 0.01

also the case for the nonionic/g-CN compared to the nonionic polymer (see Fig. S4(b)). The peak indicates the dominance of certain pore sizes in percentages. For PIL/g-CN, the most frequently occurring pore size is observed between 1.5 and 2 μm, similarly for PIL with 1.8 to 2 μm, however less frequently. The results from this investigation highlight significant variations in pore size, particularly in the PIL/g-CN composite membrane. For the PIL/g-CN membrane, the measurements indicated a minimum pore size of 0.48 μm, reflecting the smallest detectable through pore. On the other end of the spectrum, the maximum pore size was found to be 12.62 μm (Fig. S2 and S3). This range suggests a broad distribution in pore sizes, which can impact the membrane's filtration characteristics, including permeability and selectivity.

2.3.3 Surface wetting properties. The water contact angle (CA) of membranes (static, as well as advancing and receding (ARCA)) are presented in Table 3 along with the hysteresis values (difference between advancing and receding CAs) (see Materials and methods, section ''Contact angle measurements'' for the details of the experiments).

All membranes exhibit moderate hydrophilicity, with static contact angles ranging from approximately 56 to 63. Generally, a lower static CA indicates a more hydrophilic surface, which is beneficial for applications requiring high water permeability and antifouling properties. The nonionic polymer shows the lowest static CA (56.52), indicating it is slightly more hydrophilic compared to the other samples. Adding g-CN to the membranes generally increases the static CA, indicating a slight decrease in hydrophilicity. For instance, the nonionic/g-CN membrane has a higher static CA (63.70) compared to the nonionic polymer.

The PIL/g-CN membrane maintains a balance with a static CA of 61.76 and moderate hysteresis values (35.64), providing insight into surface roughness and chemical heterogeneity.[51] The higher hysteresis measured here for all membranes, indicates more surface irregularities or mixed hydrophobic/hydrophilic regions. The PIL polymer shows the highest hysteresis (38.08), suggesting significant surface roughness or heterogeneity, which might affect its wettability and fouling behavior.

All in all, the membranes have similar hydrophilic properties, with the ionic membranes exhibiting greater hydrophilicity. The hydrophilic nature of the membrane is important because it makes it more permeable to water. This is evident in PIL matrix due to the repeating units of ionic liquids and a charge separation that causes a high degree of electrostatic interaction with the water molecules. The hydrophilicity of a membrane also increases the antifouling properties.

2.3.4 Membranes' permeability and permeance. Fig. 6a demonstrates the flux of permeating pure water through membranes at different pressure values.

The pure water permeability of membranes is calculated using the integrated form of the Darcy's law[52]

$$Q = \frac{\kappa A}{\mu}\frac{\Delta p}{L}, \tag{5}$$

where Q is the total volumetric flow rate of permeating fluid (water) ($m^3\ s^{-1}$), κ is membrane permeability (m^2), A is the total membrane area (m^2), μ is the viscosity of permeating fluid (Pa s), Δp is the pressure difference, and L is the length in the flow direction, *i.e.*, membrane thickness (m).

The permeating water flux continues to increase significantly with pressures for all the membranes. This is inline with the linear relation between flux (Q/A) and the pressure difference (ΔP) based on the Darcy's law (eqn (5)).

To better compare the permeability values of the membranes, the thickness effect should be excluded. To do so, membrane permeance or pressure-normalized flux is calculated using

$$J = \mathrm{Pe} \times \Delta p, \tag{6}$$

where (J) ($L\ m^{-2}\ h^{-1}$) is the flux of permeating water through the membrane, Pe is the membrane permeance (pressure-normalized flux) ($L\ m^{-12}\ h^{-1}\ bar^{-1}$), and ($\Delta p$) (bar) is the applied pressure difference.

Pure water permeance of the membranes at a pressure of 0.7 bar is illustrated in Fig. 6b. The addition of g-CN to the PIL matrix results in a remarkable increase in water permeance. The PIL/g-CN membrane shows a 77% higher permeance

Table 3 Static and advancing-receding water contact angle measurements on ionic and nonionic membranes using water as the wetting liquid (the values after ± shows the standard deviation from 6 measurements)

Samples	Mean static (°)	Advancing (°)	Receding (°)	CA hysteresis (°)
Nonionic polymer	56.52 ± 0.16	59.76 ± 0.37	23.78 ± 0.72	32.74 ± 0.72
PIL polymer	58.77 ± 3.84	69.01 ± 0.12	51.00 ± 0.22	38.08 ± 0.83
PIL	60.63 ± 3.68	71.86 ± 0.18	36.49 ± 0.37	35.37 ± 0.80
PIL/g-CN	61.76 ± 0.86	63.05 ± 0.19	27.41 ± 0.58	35.64 ± 0.96
Nonionic/g-CN	63.70 ± 0.13	68.99 ± 0.87	30.35 ± 0.15	33.35 ± 0.28

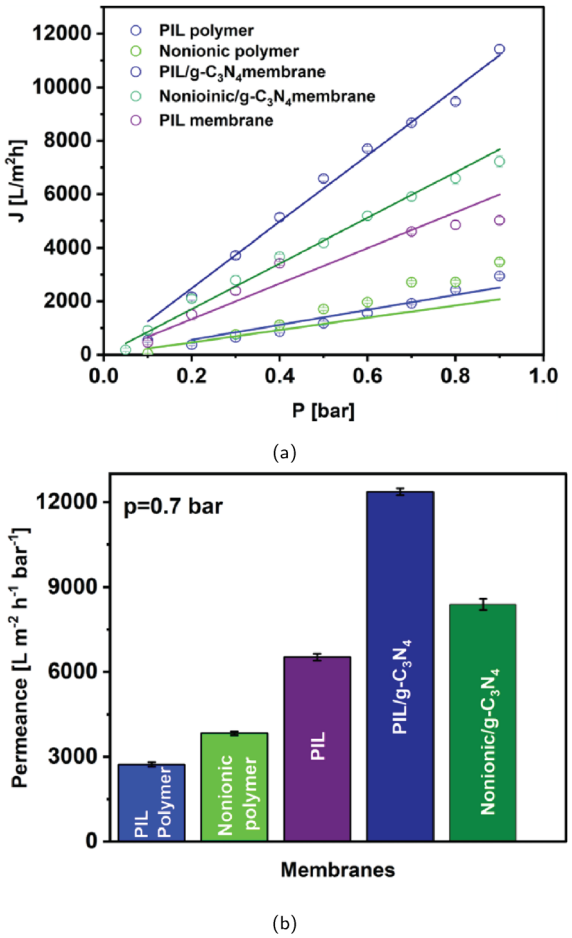

Fig. 6 (a) Permeating water flux through all the membranes *versus* applied pressure. (b) Pure water permeance of all the fabricated membranes at p = 0.7 bar.

compared to the PIL membrane alone and 47% higher than the PIL polymer matrix. This improvement is evidenced from the contact angle measurements (Table 3), which show that g-CN enhances the hydrophilicity of the membrane. Enhanced hydrophilicity facilitates better water interaction and transport through the membrane. The incorporation of g-CN likely modifies the membrane structure, creating more efficient pathways for water flow.

Similarly, the nonionic/g-CN membrane shows a 54% increase in hydrophilicity compared to the nonionic polymer matrix (see Table 3), resulting in a water permeance of 8390 ± 200 L m^{-2} h^{-1} bar^{-1}. g-CN makes the nonionic polymer matrix more hydrophilic, thereby facilitating better water permeation. PIL-based membranes inherently exhibit better water permeance compared to nonionic ones due to their ionic nature. Electrostatic interactions within PIL can create channels that favor water transport.

PIL membranes have higher swelling capacities driven by the electrostatic repulsion of bound charges and imbalanced permeation between the interior and exterior of PIL. For PIL membranes, the consistency of the polymer chain with solvent molecules and the dissociation of ionic groups contribute to a high swelling capacity, as shown in Table 1. This swelling increases the effective pore size and improves water flux. The rich R groups on the imidazolium cation in PIL offer the possibility of fine-tuning the swelling capacity, thereby optimizing water permeance.

Note that the PIL membrane prepared with an antisolvent has a lower permeance than the PIL/g-CN membrane, but a higher permeance than the PIL polymer alone. This is probably due to the partial improvement of the membrane structure and hydrophilicity by the antisolvent, which improves the water transport pathways but not to the same extent as the PIL/g-CN membrane. The addition of the antisolvent can increase porosity and improve the surface properties of the membrane, resulting in better water permeability than the pure PIL polymer. However, it does not provide the same level of structural modification and hydrophilicity improvement as g-CN, resulting in lower permeability compared to PIL/g-CN.

PIL/g-CN membrane has a significantly higher permeance value of 12 369 L m^{-2} h^{-1} bar^{-1} than PIL polymer with permeance value of 2731 L m^{-2} h^{-1} bar^{-1}. The nonionic polymer membrane exhibits lower permeability than the nonionic/g-CN membrane and the absence of g-CN triggered a decrease in the water permeance. This is inline with the pore size distribution measurements as the nonionic membranes show smaller pore size distribution compared to the nonionic/g-CN membrane (See SI, Fig. S4 for pore size distribution of all fabricated membranes).

There is a clear positive correlation between increased pore sizes and increased permeance. The introduction of g-CN to the PIL membrane significantly enhances both the pore sizes and the permeance. This observation emphasizes the important role of g-CN in improving the ionic properties of PIL, making the composite membrane more hydrophilic and selective, as also reported by Cao *et al.*[50]

Similar to the PIL membranes, adding g-CN to the nonionic matrix results in an increase in mean and maximum pore sizes (Table 2), correlating with an increase in permeance. The maximum pore size increased from 9.25 ± 1.22 μm (nonionic polymer) to 12.63 ± 0.01 μm (nonionic/g-CN). However, the smallest pore size shows a slight decrease. Larger pore sizes generally result in higher permeance, indicating that the structural modification of membranes by incorporating g-CN enhances their permeability. This phenomenon is consistent with previous results for water contact angle demonstrating the beneficial influence of g-CN on membrane properties.[50]

2.3.5 Membranes' adsorption performance. The UV calibration curve and UV-Vis absorption of methylene blue (MB) on at least three PIL membranes, in the presence and absence of the g-CN, are obtained by doing the experiments for 120 min at 25 °C (The UV-Vis spectrum of MB, and the corresponding calibration curve are shown in the SI, Fig. S10).

The adsorption experimental data are fitted using various kinetic models, namely, pseudo-first-order (PFO), pseudo-second-order (PSO), Elovich, and intra-particle diffusion (IPD), to obtain key parameters such as adsorption capacity, equilibrium constants, and further get insights into adsorption

Table 4 Kinetic parameters of MB adsorption using PIL membrane and PIL/g-CN membrane as the adsorbent obtained by fitting to various kinetic models. q_e is the amount of adsorbed MB or adsorption capacity at equilibrium, k_1 is the rate constant of the pseudo-first-order model, k_2 is the rate constant of the pseudo-second-order model, α is the initial adsorption rate, and β is the desorption constant obtained from the Elovich model, k_{id} is the intra-particle diffusion rate constant, and C is the fitting intercept. R^2 shows the goodness of the fit and χ^2 describes the dependency between the experimental and the fitted values

Adsorbate-membranes	MB-PIL	MB-PIL/g-CN
Experimental		
q_e (mg g^{-1})	21.62	17.92
Pseudo-first-order		
q_e (mg g^{-1})	21.79 ± 0.73	17.44 ± 1.48
k_1 (1 min^{-1})	5.41 ± 0.50	2.39 ± 0.49
χ^2	1.24	2.91
R^2	0.98222	0.93301
Pseudo-second-order		
q_e (mg g^{-1})	24.86 ± 1.61	21.00 ± 1.96
k_2 (g mg^{-1} min^{-1})	0.26 ± 0.07	0.12 ± 0.04
χ^2	2.58	1.73
R^2	0.95845	0.95508
Elovich		
α (mg g^{-1} min)	337.54 ± 176.00	84.50 ± 20.33
β (g mg^{-1})	0.20 ± 0.04	0.19 ± 0.03
R^2	0.90734	0.96822
Intra-particle diffusion		
k_{id} (mg g^{-1} min$^{-1/2}$)	15.67 ± 3.50	12.80 ± 1.15
C (mg g^{-1})	4.64 ± 2.41	1.34 ± 0.85
R^2	0.74065	0.95347

mechanisms. This analysis helps understand the relationship between initial dye concentrations and adsorption performance, and the suitability of PIL/g-CN membranes for treating real wastewater contaminated with MB dye. The details of each model and the corresponding equations are detailed in the SI, section ''Adsorption experiments''.

The adsorption kinetic parameters obtained by analyzing the adsorption experimental data using kinetic models and non-linear regression methods are listed in Table 4. The corresponding adsorption plots are illustrated in Fig. 7. The comparison between experimental and calculated adsorption capacities (q_t values) is shown in Fig. 7a and b. The pseudo-second-order (PSO) fit to the linearized plot of t/q_t *vs.* time is presented in the SI, Fig. S11.

The kinetic parameters in Table 4 provide insights into which kinetic model best fits the experimental data. A R^2 value closer to 1 indicates a better fit of the model to the data. As the χ^2 describes the discrepancy between the observed and expected values, a lower value indicates a better fit of the model to the experimental data.

Table 4 further shows that the pseudo-first order (PFO) and pseudo-second-order (PSO) kinetic models fit the experimental data of MB adsorption on PIL membranes better than other models, indicated by the high values of R^2 (0.98222 for PFO and 0.95845 for PSO) and the low values of χ^2 (1.24 for PFO and 2.58 for PSO). The dye adsorption on the PIL/g-CN membrane is best described by the Elovich model and pseudo-second-order (PSO) based on the high R^2 values (0.95508 for PSO, and 0.96822 for Elovich).

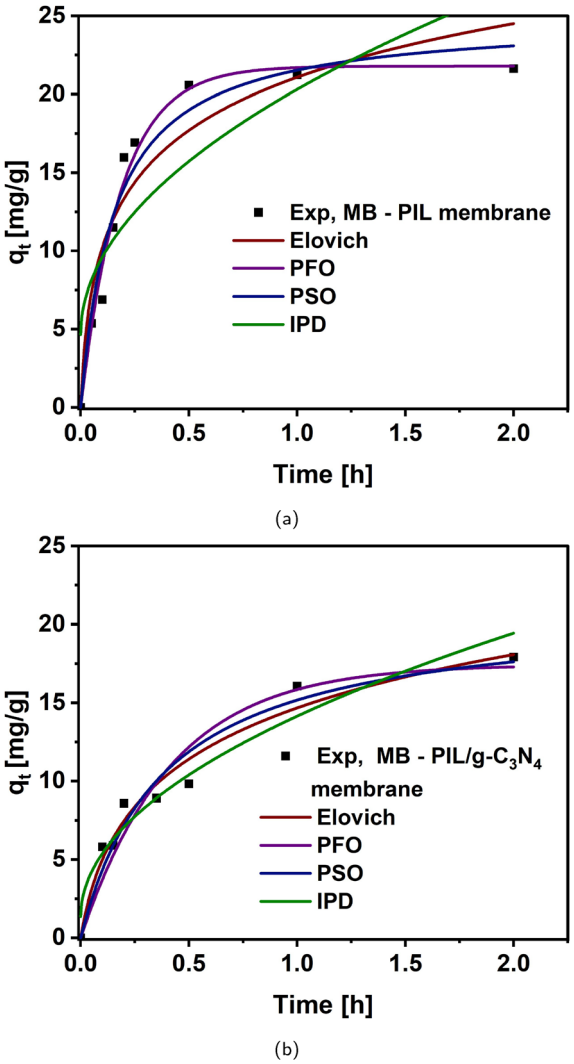

Fig. 7 Comparison of experimental and calculated adsorption capacity values (q_t) based on non-linear regression analysis of various kinetic models (pseudo-first-order (PFO), pseudo-second-order (PSO), Elovich, and intra-particle diffusion (IPD)) for adsorption of MB on (a) PIL, and (b) PIL/g-CN membranes.

The calculated kinetic parameters further demonstrate that the adsorption process for the adsorbent PIL/g-CN is mainly governed by chemisorption.[53] The high adsorption capacity further underlines the great potential of the PIL/g-CN materials for water purification as highly effective and stable adsorbents. The adsorption capacity is highest for PIL, which is due to the electrostatic attraction between the positively charged imidazolium groups and the anionic MB molecules, as reported by Atta *et al.*[54] and Zhao *et al.*[53]

2.3.6 Static methylene blue degradation. The photocatalytic activity of the PIL/g-CN membrane towards MB photodegradation in a static environment is shown in Fig. 8a, where decrease in the MB concentration is plotted as a function of time. In static condition, the membrane is in direct contact with the MB solution instead of permeating the solution continuously through the membrane (see Fig. 4).

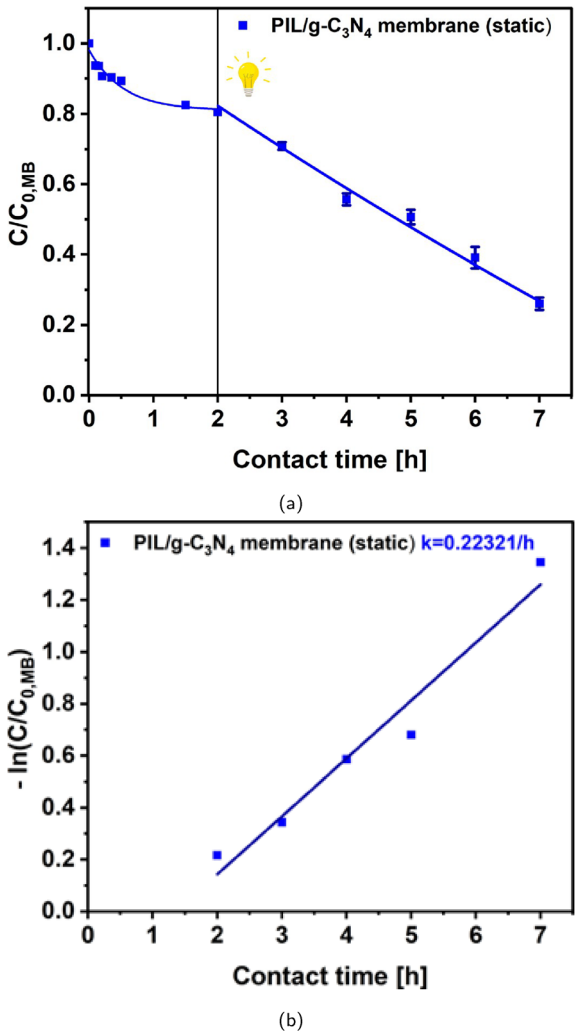

Fig. 8 Static testing of photocatalytic degradation of MB *via* PIL/g-CN. (a) C/C_0 *versus* contact time curve of photocatalytic degradation of MB. (b) Linearized C/C_0 ($\ln(C/C_0)$) *versus* contact time during degradation to calculate the rate constant k_{MB} and evaluate the membrane performance.

The irradiation, leading to MB degradation, starts after 2 h of adsorption. The MB degradation test with PIL/g-CN is carried out at least three times and with incorporated g-CN loading of 0.3 wt%. The results show the MB removal percentage of around 73.9% by the PIL/g-CN membrane. In Fig. 8b the rate constant k_{MB} = 0.22321 1 h^{-1} is obtained with a correlation coefficient R^2 of 0.95988.

Chi *et al.* reports TiO_2-modified g-CN as a photocatalyst in a PTFE composite membrane, which reduces MB using visible light, with the removal percentage of 78%.[55] Our results are inline with literature, showing effectiveness of g-CN, even with small loadings, in composite membrane for water treatment.

The reusability of the PIL/g-CN membrane is further investigated by doing cyclic adsorption-degradation experiments in three cycles. The results shown in the SI, Fig. S12, demonstrate no significant decay in the PIL/g-CN membrane efficiency as the MB removal stays constant at approximately 80% (see SI, section ''Reusability of PIL composite membranes'' for the details of the experiments). While the membrane retains its photocatalytic activity over three reuse cycles, we observed gradual shear-induced mechanical deformation at the membrane edges under continuous filtration conditions. This suggests that long-term reusability may be limited by mechanical fatigue rather than catalytic deactivation. Future work will focus on enhancing the structural robustness of the membrane to support extended operational lifetimes.

2.3.7 Continuous methylene blue degradation using dead-end filtration. In the continuous methylene blue degradation experiments using dead-end filtration, the customized membrane cell with an integrated visible light source was employed to evaluate the practical performance of the PIL/g-CN membrane (see the schematic of the membrane module in Fig. 3). This experiment is performed to assess the membrane's ability to degrade contaminants under continuous flow, and the results are shown in Fig. 9. Fig. 9a shows that the PIL/g-CN membrane achieves a removal efficiency of 47.8%, demonstrating its effectiveness in degrading methylene blue in a filtration system.

The removal percentage of the micropollutant (MB), along with the first-order kinetic rate constant (k), and the corresponding correlation coefficient (R^2) are further calculated and shown in Table 5. The rate constant k and the corresponding R^2 values for continuous MB degradation *via* filtration using the PIL/g-CN membrane are respectively 0.11 1 h^{-1} (1.9×10^{-3} 1 min^{-1}), and 0.93298, showing a good agreement between the experimental observations and the theoretical model.

The photocatalytic degradation performance of the PIL/g-CN membrane is compared with that of the nonionic/g-CN membrane tested under the same condition. The use of a nonionic/g-CN membrane in a filtration scenario resulted in a low removal efficiency of 16.1% (see Table 5).

He *et al.* reported the rate constant of 7.43×10^{-3} 1 min^{-1} with R^2 = 0.990, and 2.13×10^{-2} 1 min^{-1} with R^2 = 0.999 for MB photodegradation using g-CN and g-CN composite (6 wt% g-CN), respectively.[56] In comparison, our research utilized 0.3 wt% g-CN, achieving a rapid degradation of MB at a rate constant of 1.9×10^{-3} 1 min^{-1} with R^2 = 0.933. This indicates that even with a lower g-CN content, the PIL/g-CN membrane demonstrates good performance as a photocatalyst in polymer materials, such as PIL. This highlights the potential of PIL as an active matrix for g-CN based photocatalytic applications.

A summary of reported g-CN composites and g-CN-based membranes is presented in Table 6, highlighting the relationship between g-CN loading, water permeability, and photocatalytic dye removal performance.

The PIL/g-CN membrane with only 0.3 wt% g-CN loading, exhibits the highest reported water flux (12 369 L m^{-2} h^{-1} bar^{-1} (see Fig. 6b)), demonstrating good permeability. However, its MB removal efficiency (47.8% and 73.9% (see Fig. 8a and Fig. 9a)) and rate constant (1.9×10^{-3} 1 min^{-1}) are comparatively lower than those of most reported systems, where removal efficiencies often exceed 80%.

Most reported g-CN-based membranes use significantly higher photocatalyst loadings (6–65 wt%), are tested at higher

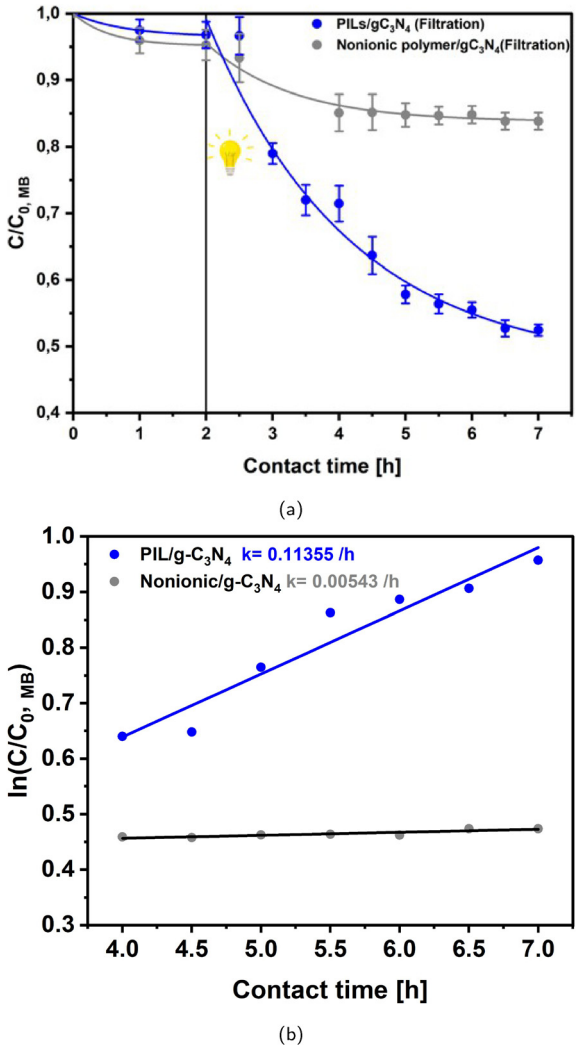

Fig. 9 Photocatalytic degradation of MB by filtration through PIL/g-CN and nonionic/g-CN membranes: (a) C/C_0 *versus* contact time curve of photocatalytic degradation of MB. (b) Linearized C/C_0 ($\ln(C/C_0)$) *versus* contact time to calculate the rate constant k_{MB} and evaluate the membrane performance.

dye concentrations (10–100 mg L^{-1}), and are typically evaluated under static (batch) conditions, with limited or no data on water permeability. While these membranes often achieve higher MB removal efficiencies, they do not combine this with similarly high water flux or low material usage.

Notably, membranes such as SPPO/g-CN achieve both high flux (8867 L m^{-2} h^{-1} bar^{-1}) and complete MB removal (100%), suggesting a more favorable balance between permeability and photocatalytic efficiency.

2.3.8 Static sulfadiazine degradation. The ^{1}H-NMR spectroscopy results of SDZ is shown in the SI, Fig. S13, demonstrating successful identification of SDZ. To assess the photocatalytic performance of the PIL/g-CN membrane for removing SDZ antibiotic from wastewater, the calibration curve of SDZ is first obtained *via* HPLC measurements (see SI, Fig. S14). The SDZ removal performance of the bare g-CN powder is subsequently investigated (see SI, Fig. S15) and the results are shown in Table 5. The results demonstrates that pure g-CN powder can remove up to 89.5% of SDZ under visible light, confirming its strong photocatalytic potential. However, using powder in filtration systems is impractical due to issues like clogging and recovery, necessitating the incorporation of the photocatalyst into membrane matrices.

Adsorption studies for SDZ are particularly challenging due to its low removal efficiency and the variability in the degradation process. As a result, it is difficult to obtain reliable adsorption data directly from the experiments. To address this, the adsorption duration is taken from literature suggestions, ensuring a standardized approach despite the experimental challenges.

The static experiments involve immersing the membrane in a SDZ solution under controlled light exposure to evaluate its ability to degrade the antibiotic in static conditions (see Materials and methods, section ''Photocatalytic degradation experiments'' for the details of the experiment). The percentage removal, along with the first-order kinetic rate constant, k, and the correlation coefficient R^2 for static and continuous degradation experiments are shown in Table 5.

PIL/g-CN membrane shows a significant reduction in removal efficiency, achieving 24.2% removal of SDZ in continuous degradation experiments *via* filtration. The rate constant (k) for the SDZ degradation of the PIL/g-CN membrane in static condition is calculated to be 4.9×10^{-4} 1 min^{-1}, with a correlation coefficient (R^2) of 0.76338. This relatively low R^2 value indicates a poor fit of the kinetic model to the experimental data, suggesting variability and potential inefficiencies in the photocatalytic degradation process for SDZ using the PIL/g-CN membrane. These findings highlight the need for further optimization to improve the membrane's performance in antibiotic removal for wastewater treatment applications.

Table 5 Photocatalytic degradation of the studied micropollutants (MP), namely MB and sulfadiazine (SDZ), by the membranes in static degradation and continuous degradation experiments using membrane filtration. R is percentage removal of the micropollutant, k is the first-order rate constant, and R^2 is the corresponding correlation coefficient

MP-Membrane-Process	R (%)	k (1 h^{-1})	k (1 min^{-1})	R^2
MB-PIL/g-CN-static	73.9	0.22 ± 0.03	$3.7 \times 10^{-3} \pm 4.0 \times 10^{-4}$	0.95988
MB-PIL/g-CN-filtration	47.8	0.11 ± 0.01	$1.9 \times 10^{-3} \pm 2.0 \times 10^{-4}$	0.93298
MB-Nonionic/g-CN-filtration	16.1	0.005 ± 0.001	$9.05 \times 10^{-5} \pm 2.03 \times 10^{-5}$	0.79937
SDZ-pure g-CN-static	89.5	0.29 ± 0.03	$4.9 \times 10^{-3} \pm 5.0 \times 10^{-4}$	0.95768
SDZ-PIL/g-CN-static	18.3	0.03 ± 0.01	$4.9 \times 10^{-4} \pm 1.59 \times 10^{-4}$	0.76338
SDZ-PIL/g-CN-filtration	24.2	0.001 ± 0.0005	$2.0 \times 10^{-5} \pm 9.1 \times 10^{-6}$	0.70196

Table 6 Comparison between the results obtained in this work and the previous studies on composite g-CN-based membranes for photodegradation of organic dyes, *e.g.*, methlyene blue (MB), and rhodamine B (RhB). The abbreviations and additional information for each membrane are as the following. (1) Polyethersulfone membrane with zirconium dioxide nanocomposite of graphitic carbon nitride, (2) zinc oxide-graphitic carbon nitride composite membrane, (3) fibrous polyvinylidene fluoride membranes with graphitic carbon/graphene oxide (GO) composite (concentration of g-CN: 3 wt%), (4) nanocomposite of graphitic carbon nitride with reduced graphene oxide (rGO) and nickel sulfide (NiS) incorporated into GO membrane (Concentration of nanocomposite: 15 wt%), (5) graphitic carbon nitride membranes based on self-assembled photo-Feton-like membranes (Fe-containing polyoxometalates (Fe-POMs)), (6) polyoxometalate (POMs) functionalized g-CN (POMs@g-CN) obtained *via* hydrothermal method using $PMo_{12}O_{40}{\cdot}xH_2O$ with POM loading of 6 wt%, (7) sulfonated poly(2,6-dimethyl-1,4-phenylene oxide) composite membranes with graphitic carbon nitride, and (8) poly ionic liquid composite membrane with 0.3 wt% graphitic carbon nitride

Membrane type	Pure water flux (L m^{-2} h^{-1} bar^{-1})	Dye concentration (mg L^{-1})	Dye removal efficiency (%)	Rate constant (1/min)	Ref.
PES/CNGZ[1]	15.7	10	MB (self forming): 89%	12.5×10^{-3}	57
ZnO/g-CN[2]	336.8	15	MB: 94.4	NA	58
PVDF/g-CN@GO[3]	NA	10	RhB: 60%	26×10^{-3}	59
g-CN/rGO/NiS[4]	NA	100	MB: 90%	9.1×10^{-3}	60
g-CN/Fe-POMs[5]	42.5	10	MB: 99.1%	NA	61
PMo_{12} @g-CN[6]	NA	10	MB: 80%	21.3×10^{-3}	56
SPPO/g-CN[7]	8867	NA	MB: 100%	NA	62
PIL/g-CN[8]	12 369	3 (filtration) 10 (static)	MB: 47.8% (filtration) 73.9% (static)	1.9×10^{-3}	This work

2.3.9 Continuous sulfadiazine degradation using dead-end filtration. To further evaluate the practical application of the PIL/g-CN membrane for antibiotic removal, continuous SDZ degradation experiments were conducted using a dead-end filtration setup (see Fig. 3). The results are shown in Fig. 10, demonstrating an increase in the removal efficiency of SDZ from 8.8% in static condition to 18.5% in continuous condition *via* filtration (Fig. 10a).

Fig. 10b SDZRemovalPIL illustrates that despite the absorptive properties of the PIL, which enhance MB adsorption, it does not lead to a significant decrease in SDZ concentration. This suggests that the adsorption process alone is inadequate for effectively reducing SDZ levels. However, when employing the PIL/g-CN membrane for degradation, a noteworthy decline in SDZ concentration within the solution is observed. Specifically, after 24 hours, SDZ levels are diminished by up to 24%, as depicted.

2.3.10 Membranes' antifouling performance. Membrane fouling is explored using sodium alginate (SA) as a hydrophilic organic substance. The antifouling properties of the membranes are assessed *via* two methods and fouling mechanisms. The membrane fouling caused by SA manifested in two ways: (1) the formation of a dense cake layer on the membrane's surface, and (2) the formation of alginate beads *via* SA solution with $CaCl_2$, on both the membrane's surface and within its pores. The corresponding fouling mechanisms are (1) cake formation *via* dense SA layer, and (2) pore blocking, which occurs in the initial phases of the filtration process.

The antifouling experiments are operated in dead-end filtration mode to understand the changes in the permeate flux (J) (see Materials and methods, section "Antifouling experiments" for the details of the experiment). The SEM images of the surface of PIL and PTFE membranes are shown in the SI, Fig. S16. During membrane filtration, an increase in the transmembrane pressure (TMP) or a decrease in flux is an indication of membrane fouling.[63] In this work, the changes in the permeate flux (J), using eqvolu in Section 2.2.10, along with

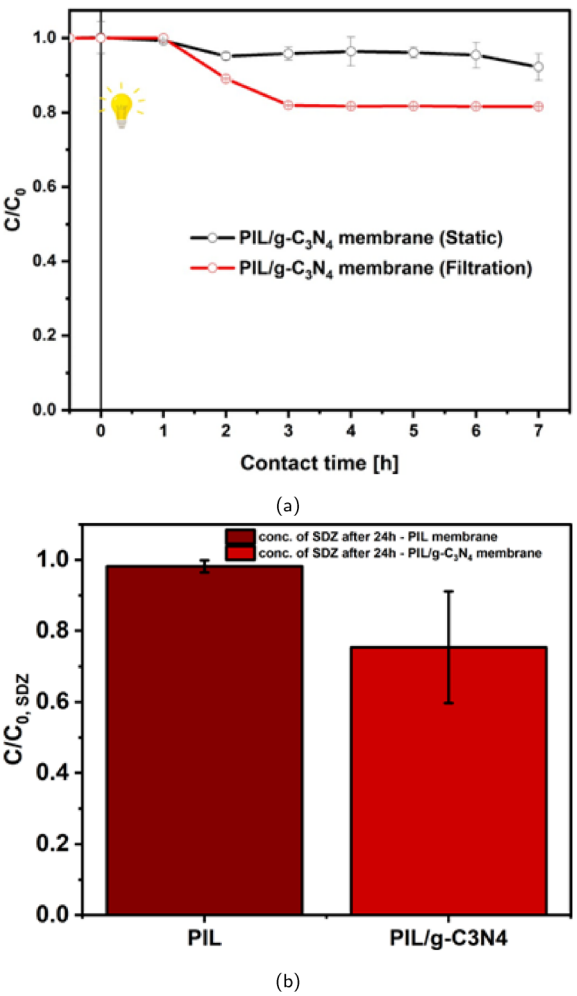

Fig. 10 Photocatalytic degradation of SDZ by PIL/g-CN and PIL membranes. (a) C/C_0 *versus* contact time curve of photocatalytic degradation of SDZ *via* PIL/g-CN membrane in both static approach and continuous approach using filtration. (b) Photocatalytic degradation of SDZ after 24 h of light irradiation *via* PIL/g-CN and PIL membranes.

the visual observation of the membrane surface using SEM after filtration of the fouling medium, are investigated. The fouling process is evaluated on two membranes, namely the fabricated PIL membrane and the commercially available hydrophilic microfiltration PTFE membrane.

Membrane performance in filtering sodium alginate beads. The normalized flux decrease upon filtration of the solution containing SA beads through the PIL and PTFE membranes are shown in Fig. 11c. The corresponding values of the normalized flux decrease (J/J_0), along with the flux decrease rate (k_J) and the stabilized values of the J/J_0 are shown in the SI, Table S2 and Fig. S17. The SEM images presented in Fig. 11a and b illustrate the fouling patterns after filtering SA bead solution through PTFE membrane and PIL membranes, respectively. The images show spherical deposits on the membrane surfaces. The deposited SA beads on the PIL membrane surface after filtration show a smaller particle size (Fig. 11b) compared to those on the PTFE membrane surface Fig. 11a.

The particle size of SA beads on PTFE membrane (Fig. 11a) is approximately 2 μm, while the particle size of the SA beads deposited on PIL membrane (Fig. 11b) is smaller than 1 μm. PTFE membrane has an average pore diameter of around 10 μm and the fabricated PIL membrane has a maximum pore diameter of 8.4 μm (see Table 2).

The presence of larger SA particles on the surface of PTFE membranes, together with a higher flux decrease of 48% (Table S2 and Fig. 11c), indicates that hydrophilicity alone is not sufficient to prevent fouling. The ionically charged surface of the PIL enhances antifouling performance, contributing to a 33% reduction in flux. Dai *et al.*[64] and Wylie *et al.*[65] describe the formation of a dense hydration layer on the PIL membrane surface, which creates an affinity for water molecules and reduces the adhesion of biofouling. Dai *et al.*[64] particularly emphasizes the interactions between PIL and hydrophobic polyphenylene sulfone ultrafiltration membranes prepared by the nonsolvent induce phase separation (NIPS) method, which lead to improved surface hydrophilicity.

At the molecular scale, the antifouling characteristics of poly(ionic liquids) (PILs) arise from the high density of ionic functionalities, typically imidazolium, pyridinium, or phosphonium, distributed along the polymer backbone, which confer strong surface charge and pronounced hydrophilicity.[65,66] These charged moieties promote the formation of an interfacial hydration layer, composed of tightly bound water molecules stabilized by electrostatic and hydrogen bonding interactions.[67]

This structured water layer serves as a steric and energetic barrier, significantly impeding the approach and adhesion of potential foulants by increasing the thermodynamic cost associated with dehydration and direct surface contact. In parallel, electrostatic repulsion between the positively charged PIL surface and similarly charged contaminants further reduces nonspecific adsorption and aggregation.[67] The dynamic nature of the PIL backbone permits rearrangement of side chains, allowing the membrane surface to maintain hydration coverage even under flow or mechanical stress.[65,66]

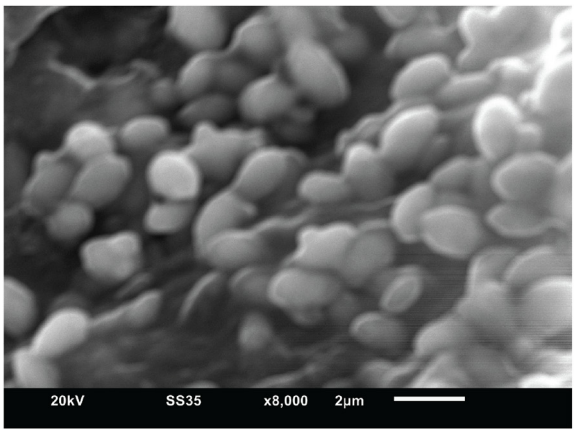

(a)

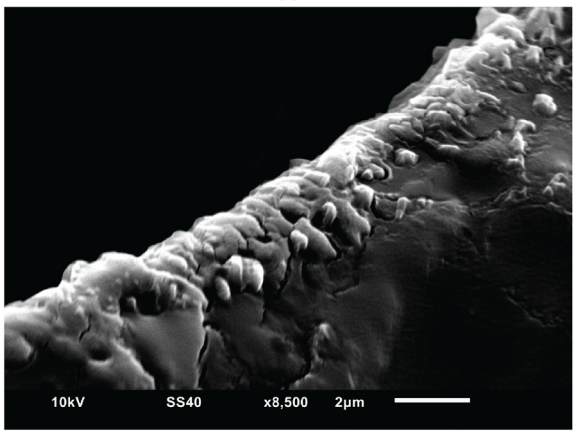

(b)

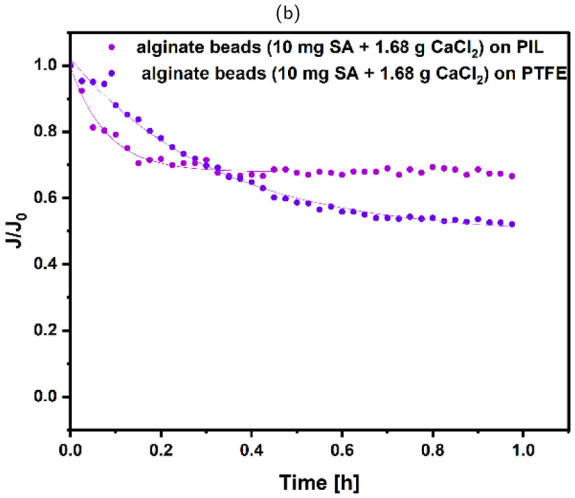

(c)

Fig. 11 SEM images showing SA beads on (a) PTFE and (b) PIL membrane after filtration of solution containing SA beads. (c) Flux decreases after filtering the same solution through PIL and PTFE membranes. J is the membrane flux(L m^{-2} h^{-1}) over time t and J_0 represents the initial membrane flux (L m^{-2} h^{-1}).

These findings have been confirmed by antifouling tests on PIL-functionalized membranes such as SIL-Br and SIL-Pro, which exhibit significantly reduced protein adhesion, enhanced resistance to biofouling, and sustained water flux

performance compared to non-PIL-functionalized poly(2-dimethylaminoethyl methacrylate)-*block*-polystyrene (PDMAEMA-*b*-PS) membranes.[67] Note-worthily, the modular chemistry of PILs allows fine-tuning of interfacial properties through variation in side chain length, ionic group identity, and counter-ion selection, providing a versatile platform for optimizing antifouling behavior.[66]

Membrane performance in filtering sodium alginate solution. Fig. 12c shows the flux decrease after permeating 5 mg L^{-1} and 10 mg L^{-1} of SA model foulant solution through PTFE and PIL membranes, leading to layer formation on the membrane surface. The corresponding values of the normalized flux decrease, the flux decrease rate, and the stabilized values of the J/J_0 are shown in the SI, Table S2, and Fig. S17. The SEM images of this layer are depicted in Fig. 12a for PTFE, and Fig. 12b for the PIL membranes.

The initial fouling causes cake formation, while the higher the SA concentration, the lower the permeate flux due to higher cake resistances.[63] The normalized flux decrease (J/J_0) upon permeating solutions containing 5 mg L^{-1} and 10 mg L^{-1} of SA through both PIL and PTFE membranes reveals notable patterns.

In particular, during the first 10 minutes, the permeate flux for the PTFE membrane drops more sharply with the 10 mg L^{-1} SA solution compared to that of the 5 mg L^{-1} SA solution, indicating a higher fouling rate at the higher SA concentration. As filtration continues, the flux (J) stabilizes at a lower level due to the increased fouling associated with the higher concentration of SA. This observation aligns with the findings of Liu *et al.*[63]

The flux decrease rate values (k_J) are obtained for all the membranes from the linearized flux decrease ($\ln(J/J_0)$) plot as a function of time (Fig. 13).

For the PIL membranes, the 5 mg L^{-1} SA variant shows a lower flux decrease rate (0.63 1 h^{-1}) compared to that of the 10 mg variant (1.71 1 h^{-1}) (see SI, Table S2), suggesting a faster fouling process at higher SA concentrations (Fig. 13b). PTFE membranes exhibit higher flux decrease rates compared to PIL membranes after filtering SA solutions. The high filtration rates observed in PTFE membrane filtered with 5 mg L^{-1} SA at 4.33 1/h suggest high permeability, as illustrated in Fig. 13a. The lowest filtration rate is given in Fig. 13c, indicating a gradual and consistent fouling process on the membranes. PTFE membrane exhibits a more rapid decline in performance.

The PIL membrane demonstrated superior antifouling properties compared to the PTFE membrane due to its ionic nature. The PIL membrane experienced significantly less fouling at all concentrations, suggesting that ion-based membranes like PIL outperform commercial PTFE membranes in resisting biofouling.

Pore-blocking analysis using Hermia's model. One of the most broadly utilized models for membrane fouling is the Hermia's model to simulate fouling tendencies in water treatment systems. By determining specific model coefficients k for different operational conditions, the model has demonstrated accuracy, suggesting its capability to effectively characterize fouling tendencies in such systems.[68]

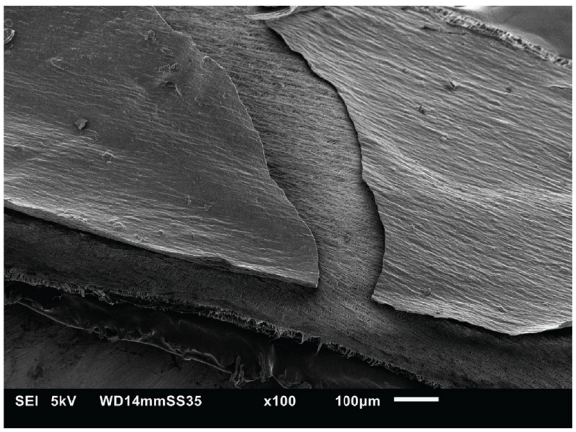

(a)

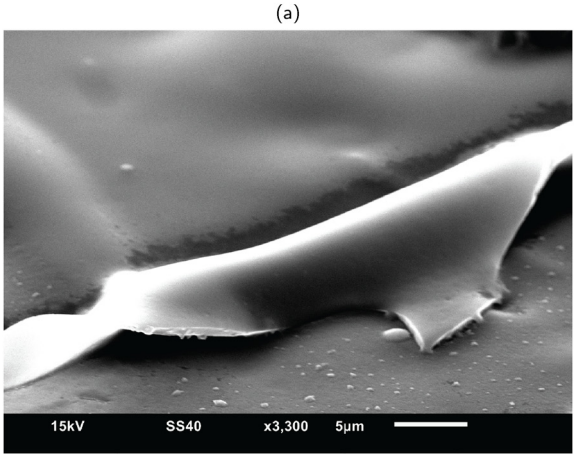

(b)

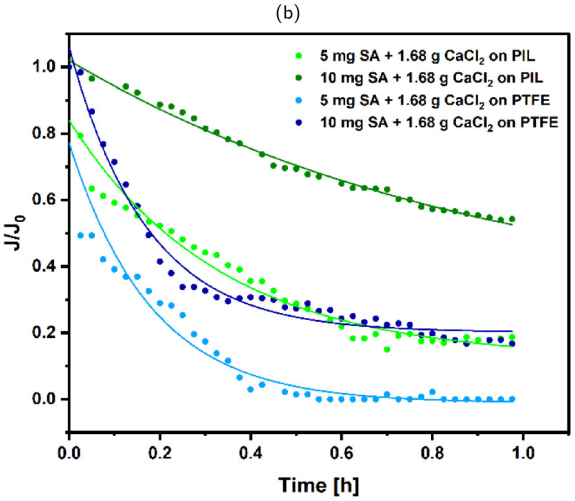

(c)

Fig. 12 SEM images showing SA layer formed on (a) PTFE and (b) PIL membrane after filtration of 10 mg L^{-1} SA solution. (c) Flux decrease after filtering 5 mg L^{-1}, and 10 mg L^{-1} SA model foulant solutions through PIL and PTFE membranes. J is the membrane flux(L m^{-2} h^{-1}) over time t and J_0 represents the initial membrane flux (L m^{-2} h^{-1}).

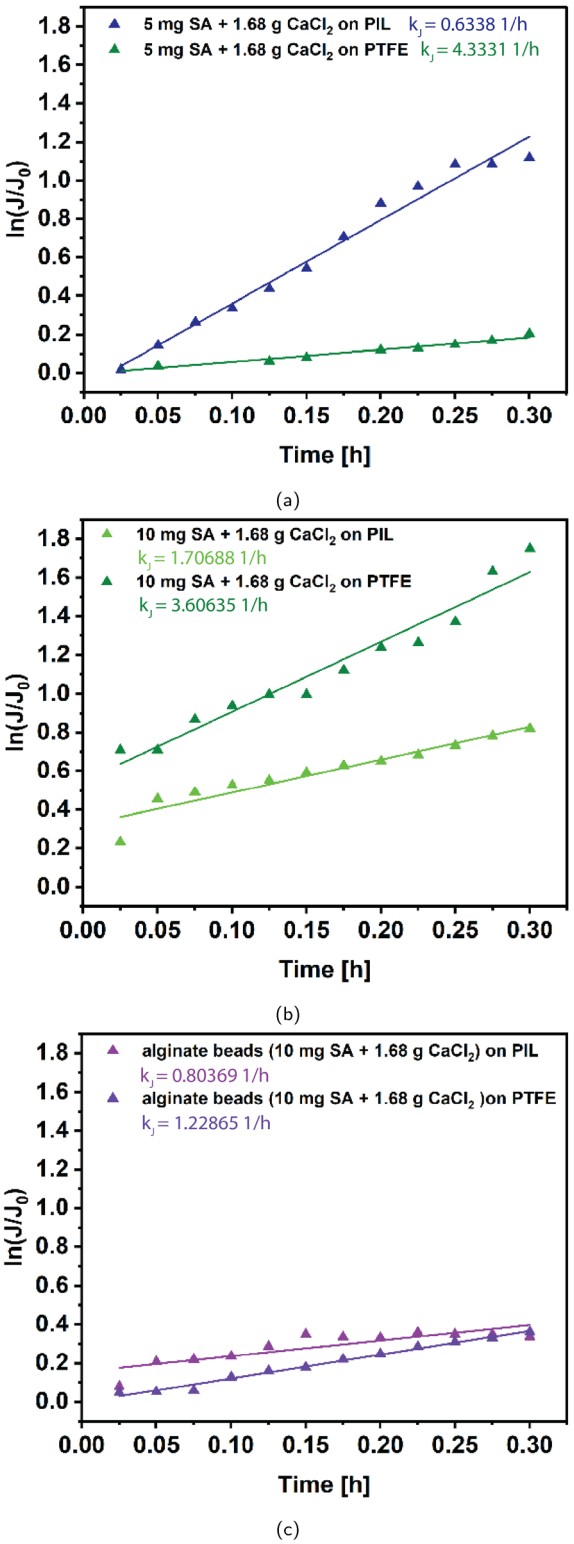

Fig. 13 $\ln(J/J_0)$ *versus* time (h) to determine the flux decrease rate (k_J) after filtering model foulant solutions containing (a) 5 mg L^{-1} SA, (b) 10 mg L^{-1} SA, and (c) SA beads through PIL and PTFE membranes.

The flux decrease is analyzed based on the four fouling mechanisms, namely, complete blocking (CB), intermediate blocking (IB), standard blocking (SB), and cake formation (CF), developed according to the Hermia's model. The corresponding flux expressions are shown in Table 7 and the details of each model are described in the SI, section "Hermia's membrane fouling model". The results of the analysis, including the resistance coefficients and goodness of fit, for filtering SA model foulant solutions through both PIL and PTFE membranes is shown in Table 8.

Table 7 Fouling models developed based on Hermia's model and the corresponding flux expressions. "k" is the resistance coefficient with different unit for each model, and "n" is the pore blockage index, *i.e.*, a dimensionless filtration constant that depends on the state of pore blockage

Fouling model	n	Flux expression	Resistance coefficients
Complete blocking (CB)	2	$J = J_0\exp(-k_{CB}t)$	k_{CB} (1 s^{-1})
Intermediate blocking (IB)	1	$J = \frac{J_0}{1 - k_{IB}tJ_0}$	k_{IB} (1 m^{-1})
Standard blocking (SB)	1.5	$J = \frac{J_0}{(1 - k_{SB}t\sqrt{J_0})^2}$	k_{SB} (1 $ms^{-0.5}$)
Cake formation (CF)	0	$J = \frac{J_0}{\sqrt{1 - k_{CF}tJ_0^2}}$	k_{CF} (s m^{-2})

Fig. 14 illustrates a comparison between the experimental permeate flux decrease to the Hermia's fouling models to identify the fouling mechanisms. At a low concentration of SA (5 mg L^{-1}) (Fig. 14a), the standard blocking (SB) model matches the experimental results observed between t = 0 min and t = 60 min, yielding an R^2 value of 0.949 for the PTFE membrane, and 0.983 for the PIL membrane, respectively (see Table 8). However, for the PIL membrane, the complete blocking (CB) model shows a slightly better fit in terms of R^2.

Table 8 Evaluation of four fouling models used to identify the pore-blocking mechanism upon filtration of SA solutions through both the PIL and PTFE membranes. The resistance coefficient values (k values) in the Hermia's model is a real constant derived from experimental data. Each model has its own k value (see Table 7), and R^2 shows the goodness of fit. The pressure is 0.1 bar in all the analysis. The experimental data for PIL-SA beads did not adequately fit Hermia's model. Thus, these results are not presented

Membrane-foulant	Model	R^2	k value
PIL-SA 10 mg L^{-1}	CB	0.904	2.474
	IB	0.965	4.746
	SB	0.958	1.721
	CF	0.911	17.899
PIL-SA 5 mg L^{-1}	CB	0.987	0.655
	IB	0.973	0.824
	SB	0.983	0.368
	CF	0.942	2.062
PTFE-SA 10 mg L^{-1}	CB	0.944	6.476
	IB	0.887	15.680
	SB	0.936	4.975
	CF	0.743	85.355
PTFE-SA 5 mg L^{-1}	CB	0.897	2.600
	IB	0.947	4.846
	SB	0.949	1.790
	CF	0.874	17.527
PTFE-SA beads	CB	0.899	0.854
	IB	0.963	1.161
	SB	0.939	0.499
	CF	0.975	3.114

The results given in Fig. 14b demonstrate that employing a higher concentration of SA solution (10 mg L^{-1}) accelerates membrane fouling. The fitting to data obtained from filtration with the PIL membrane aligns well with both the standard blocking model (R^2 = 0.958) and the intermediate blocking model (R^2 = 0.965).

The k value in the Hermia's model is a real constant derived from experimental data, used to describe different fouling mechanisms during filtration. For standard blocking, this parameter represents the decrease in the cross-sectional area of the membrane pores per unit permeate volume.[69] The k value obtained from fitting the standard blocking model to the experimental results of filtering 10 mg L^{-1} SA solution through the PIL membrane is the lowest (k_{SB} = 1.721 1 $ms^{-0.5}$), indicating pore blocking within the cross-section of the membrane.

In Fig. 14c, the experimental data is shown from filtering a solution containing SA beads at a concentration of 10 mg L^{-1}, along with the corresponding fitting data to the four different fouling blocking mechanisms. The experimental data for the PTFE membrane in this study demonstrate a strong fit with the cake formation (CF) model, yielding a coefficient of determination R^2 = 0.975. This result is in close agreement with a previously reported study by Charfi *et al.*, where the CF model achieved an R^2 of 0.9923, indicating comparable model performance and consistency across studies.[49] This implies that fouling ascribed to SA beads likely occurs within one phase, potentially due to the formation of a cake layer on the membrane surface as a dominating factor.[49] It is worth noting that good fitting results are not obtained for the experimental flux values obtained from filtering SA beads through PIL membrane. Thus, the results are not shown in Table 7.

The fitting to the fouling mechanism models highlights the significant influence of SA concentration and the type of foulant agent (SA solution and SA beads). At higher SA concentrations, the likelihood of SA chain aggregation increases, resulting in greater rejection rates compared to lower concentrations. This increased rejection promotes the deposition of SA on the membrane surface. Conversely, lower SA concentrations lead to the dispersal of negatively charged SA chains, allowing them to migrate within the membrane pores. This process can initiate an initial fouling phase characterized by pore constriction, followed by a subsequent phase of SA deposition on the membrane surface. Over time, the formation of a cake layer may accelerate due to the gradual reduction in membrane pore size, which hampers the passage of SA chains through the membrane.

The type of foulant also play a key role. SA solutions cause fouling through both pore constriction and surface deposition based on concentration, while SA beads mainly cause surface fouling through physical blockage and inability to penetrate membrane pores. Among the various models examined, the cake formation model for filtering alginate beads (SA beads 10 mg L^{-1}) through PTFE membrane, with k_{CF} =3.114, and R^2 = 0.975, exhibited the closest agreement with the experimental data, highlighting the predominant role of cake accumulation in fouling mechanisms within this system.[70]

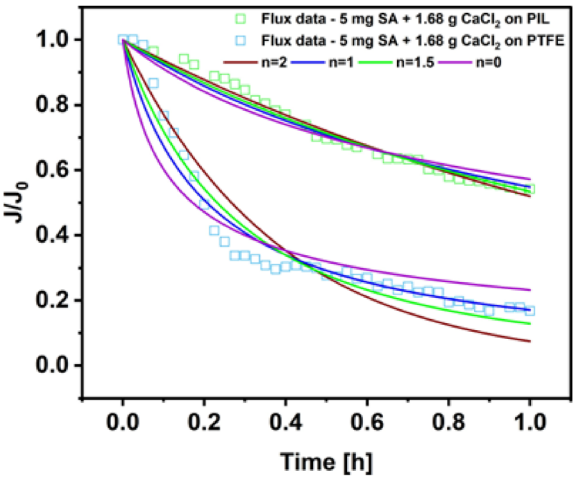

(a)

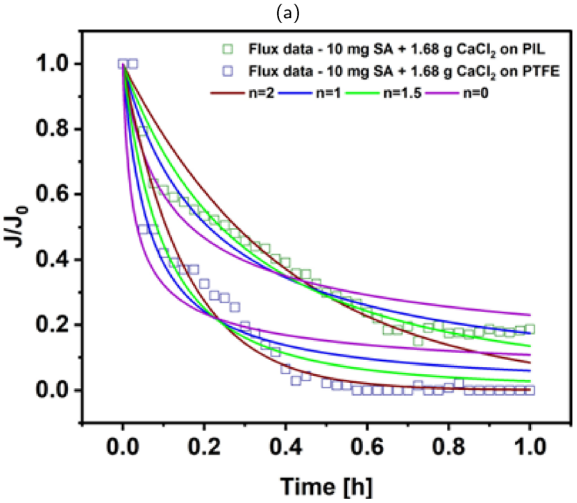

(b)

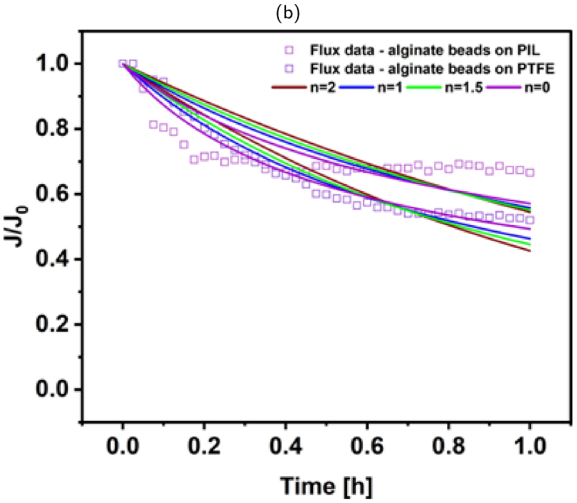

(c)

Fig. 14 Fitting of fouling models (complete blocking with n = 2, intermediate blocking with n = 1, standard blocking with n = 1.5, and cake formation with n = 0) to the normalized flux decrease results obtained from dead-end filtration of (a) 5 mg L^{-1} of SA solution, (b) 10 mg L^{-1} of SA solution, and (c) SA beads with concentration of 10 mg L^{-1} through PIL and PTFE membranes.

One constraint of Hermia's models is their assumption that certain process parameters, such as bulk concentration, transmembrane pressure (TMP), and temperature, remain unchanged throughout filtration. While maintaining constant TMP and temperature is feasible *via* feedback control, controlling bulk concentration is often impractical.

Our fitting and analysis reveal that despite these constraints, Hermia's models can still provide valuable insights into fouling behavior. Achieving reasonable model accuracy involves identifying specific coefficients for each operating point and using them for predictions. This indicates that the model framework can effectively characterize the fouling behavior of the membrane under given operating conditions. Hermia's models can reliably predict fouling when TMP and temperature are controlled, even if bulk concentration varies. This highlights the models' practical utility for understanding and predicting fouling trends, emphasizing the need for accurate coefficient determination for specific conditions.

Conclusions

This study offers a thorough exploration of the potential uses and performance enhancements of nanocomposite poly(ionic liquid) membranes *via* incorporating graphitic carbon nitride (g-CN) as photocatalytic filler. The investigation of membrane properties reveals significant improvements in porosity, permeability, hydrophilicity, and pore size distribution upon incorporation of g-CN. Photocatalytic property of membrane is harnessed *via* methylene blue dye and sulfadiazine antibiotic degradation under visible light, with promising methylene blue removal percentages exceeding 70% and stability over 3 cycles.

Effect of PIL matrix on charge transport is noted *via* photocatalytic degradation processes, which is not observed when non-charged matrix is used. To further assess the potential of the so-formed membrane in continuous processes (*e.g.*, membrane filtration with simultaneous degradation), light embedded filtration module was engineered and micropollutant removal efficiencies ranging from 10% to 30% are observed.

An important aspect of this study is to highlight the multifunctionality of the fabricated membrane and its potential environmental applications. This is further demonstrated through the antifouling experiments, which showcases the membrane's ability to resist fouling. The antifouling experiments and the corresponding evaluation using Hermia's fouling models provide valuable insights into the superior performance of the PIL membranes compared to the commercial membranes such as PTFE.

The reduced decline in flux and effective fouling mitigation suggest that PIL/g-CN membranes can potentially increase membrane longevity, which is attributed to the presence of a matrix surface charge. Although further long-term testing in cross-flow filtration is needed to fully assess the PIL membrane's performance, these initial results indicate its potential as an effective antifouling photocatalytic composite material. The hydration-mediated and electrostatic interactions form the basis of the antifouling efficacy observed in PIL-functionalized membranes and support their continued development for next-generation water treatment technologies.

PIL matrix promotes charge transfer in photo-induced reactions, therefore they can be an important candidate for multifunctional membrane engineering. Further studies enhancing light adsorption towards infrared region can provide improved reactivity over enhanced membrane thickness. Recognizing the relevance of solar-driven processes for practical applications, future studies will focus on evaluating the PIL/g-CN membranes under AM 1.5G simulated sunlight using an integrated module. This will enable us to assess photocatalytic performance in realistic wastewater environments and investigate broader environmental implications such as effects on microbial diversity.

Improving photocatalyst content can alter membrane microstructure and its effect on photocatalytic conversion efficiency can be monitored. From engineering perspective, improvements towards continuous filtration setup with integrated light can grant higher conversion efficiencies. Reusability of membranes can be studied in detail to assess their performance lifetime. We believe that antifouling photocatalytic membranes can provide a solid solution towards environmental remediation applications.

Author contributions

Hannah Schimke: data curation, formal analysis, methodology, validation, and visualization for experimental part (lead); writing/original draft preparation (lead); writing/review and editing (supporting). **Baris Kumru**: conceptualization, project administration; supervision; writing/review and editing (supporting). **Hanieh Bazyar**: conceptualization (lead); project administration; supervision (lead); writing/review and editing (lead).

Conflicts of interest

There are no conflicts to declare.

Data availability

Data for this article, including [Excel and Matlab datasets for the figures and fittings, as well as the Origin files of the figures] will be openly available at [4TU repository].

Supplementary information is available. See DOI: **https://doi.org/10.1039/d5sm00441a**

Acknowledgements

H. Bazyar and B. Kumru would like to thank the Delft Bioengineering Institute for funding this project. B. Kumru further appreciates continuous support from DASML and the department of Aerospace Structures and Materials (ASM) at Faculty of Aerospace Engineering, TU Delft. The authors would like to also

thank the following people for their help on various aspect of the project. Cornel Weststeijn from the Electronic and Mechanical Support Division (DEMO) (Delft University of Technology) for providing great support in designing, constructing, and modifying the module with the integrated light source. Irem Gurbuz (Delft University of Technology, Department of Process & Energy) for assistance with the filtration set-up, discussions on membrane fabrication and filtration methods, and microscopic analyses of the fabricated membranes. Tom Meijer (Delft University of Technology, Department of Chemical Engineering) for his support with UV chamber set-up used for photopolymerization and discussions on PIL/g-CN composites. Javier Pavez Jara (Delft University of Technology, Department of Water Management) for assistance in performing HPLC measurements of reduced SDZ concentration. Dr Thanos Papageorgiou (Delft University of Technology, Department of Chemical Engineering) for support with FTIR measurements. Ana Malvis Romero (Hamburg University of Technology, Institute of Technical Biocatalysis) for assistance in membrane technology and treatment.

References

1 S. Singh and R. Jayaram, *Sustain. Water Resour. Manag.*, 2022, **8**, 146.
2 A. Shah, A. Arjunan, A. Baroutaji and J. Zakharova, *Water Sci. Eng.*, 2023, **16**, 333–344.
3 A. Tkaczyk, K. Mitrowska and A. Posyniak, *Sci. Total Environ*, 2020, **717**, 137222.
4 H. Lu, W. Feng and Q. Li, *Water*, 2022, **14**, 2476.
5 R. Sidhikku Kandath Valappil, N. Ghasem and M. Al-Marzouqi, *J. Ind. Eng. Chem.*, 2021, **98**, 103–129.
6 D. M. Warsinger, S. Chakraborty, E. W. Tow, M. H. Plumlee, C. Bellona, S. Loutatidou, L. Karimi, A. M. Mikelonis, A. Achilli, A. Ghassemi, L. P. Padhye, S. A. Snyder, S. Curcio, C. D. Vecitis, H. A. Arafat and J. H. Lienhard, *Prog. Polym. Sci.*, 2018, **81**, 209–237.
7 X. Xu, Y. Yang, T. Liu and B. Chu, *Giant*, 2022, **10**, 100099.
8 T. Wang, W. M. de Vos and J. de Grooth, *J. Membr. Sci.*, 2022, **646**, 120209.
9 M. Davies, C. Hamilton, S. Murphy and B. Tighe, *Biomaterials*, 1992, **13**, 971–978.
10 S. Rana, R. C. Thakur and H. S. Dosanjh, *Solid State Ionics*, 2023, **400**, 116340.
11 I. Bodachivskyi, C. J. Page, U. Kuzhiumparambil, S. F. R. Hinkley, I. M. Sims and D. B. G. Williams, *ACS Sustain. Chem. Eng.*, 2020, **8**, 10142–10150.
12 A. Sengupta, S. Kumar Ethirajan, M. Kamaz, M. Jebur and R. Wickramasinghe, *Sep. Purif. Technol.*, 2019, **212**, 307–315.
13 M. Kamaz, A. Sengupta, S. S. DePaz, Y.-H. Chiao and S. Ranil Wickramasinghe, *J. Membr. Sci.*, 2019, **579**, 102–110.
14 H. Zheng, G. Xu, W. Li, X. Zhang, B. Wang, L. Qin and L. Zhou, *Eur. Polym. J.*, 2024, **204**, 112710.
15 J. Yuan, D. Mecerreyes and M. Antonietti, *Prog. Polym. Sci.*, 2013, **38**, 1009–1036.
16 H. Lin, S. Zhang, J.-K. Sun, M. Antonietti and J. Yuan, *Polymer*, 2020, **202**, 122640.
17 X. Zhou, J. Weber and J. Yuan, *Curr. Opin. Green Sustain. Chem*, 2019, **16**, 39–46.
18 J. Lin, T. Su, J. Chen, T. Xue, S. Yang, P. Guo, H. Lin, H. Wang, Y. Hong, Y. Su, L. Peng and J. Li, *Chemosphere*, 2021, **272**, 129640.
19 C. A. Dunn, Z. Shi, R. Zhou, D. L. Gin and R. D. Noble, *Ind. Eng. Chem. Res.*, 2019, **58**, 4704–4708.
20 Z. Xu, T. Wu, J. Shi, K. Teng, W. Wang, M. Ma, J. Li, X. Qian, C. Li and J. Fan, *J. Membr. Sci.*, 2016, **520**, 281–293.
21 E. Erusappan, S. Thiripuranthagan, R. Radhakrishnan, M. Durai, S. Kumaravel, T. Vembuli and N. J. Kaleekkal, *J. Environ. Chem. Eng*, 2021, **9**, 105776.
22 A. Rafiq, M. Ikram, S. Ali, F. Niaz, M. Khan, Q. Khan and M. Maqbool, *J. Ind. Eng. Chem.*, 2021, **97**, 111–128.
23 M. Sakar, R. Mithun Prakash and T.-O. Do, *Catalysts*, 2019, **9**, 680.
24 S. Mondal, G. Mark, L. Abisdris, J. Li, T. Shmila, J. Tzadikov, M. Volokh, L. Xing and M. Shalom, *Mater. Horiz.*, 2023, **10**, 1363–1372.
25 I. F. Silva, R. D. F. Rios, O. Savateev and I. F. Teixeira, *ACS Appl. Nano Mater.*, 2023, **6**, 9718–9727.
26 G. Zhang, M. Zhang, X. Ye, X. Qiu, S. Lin and X. Wang, *Adv. Mater.*, 2014, **26**, 805–809.
27 S. Baluchová, S. Zoltowska, P. Giusto and B. Kumru, *ChemSusChem*, 2024, **17**, e202400618.
28 H. Li, B. Cheng, J. Xu, J. Yu and S. Cao, *EES Catal.*, 2024, **2**, 411–447.
29 H. Li, B. Zhu, S. Cao and J. Yu, *Chem. Commun.*, 2020, **56**, 5641–5644.
30 I. M. Gonzaga, R. Gonçalves, C. H. Fernandes, M. Assis, I. F. Teixeira and L. H. Mascaro, *Chemosphere*, 2024, **352**, 141315.
31 D. P. Kumar, L.-M. Nollen, A. P. Rangappa and T. K. Kim, *Environ. Res.*, 2022, **204**, 112362.
32 K. Xiao, P. Giusto, L. Wen, L. Jiang and M. Antonietti, *Angew. Chem., Int. Ed.*, 2018, **57**, 10123–10126.
33 K. Xiao, B. Kumru, L. Chen, L. Jiang, B. V. K. J. Schmidt and M. Antonietti, *Beilstein J. Nanotechnol.*, 2019, **10**, 1316–1323.
34 C. Jia, L. Yang, Y. Zhang, X. Zhang, K. Xiao, J. Xu and J. Liu, *ACS Appl. Mater. Interfaces*, 2020, **12**, 53571–53591.
35 C. Esen and B. Kumru, *Ind. Eng. Chem. Res.*, 2022, **61**, 10616–10630.
36 R. Tao, S. Yang, C. Shao, X. Li, X. Li, S. Liu, J. Zhang and Y. Liu, *ACS Appl. Nano Mater.*, 2019, **2**, 3081–3090.
37 A. M. Sudapalli, H. M. Chavan, P. M. Badani and N. G. Shimpi, *Opt. Mater.*, 2024, **152**, 115501.
38 S. Salehian, H. Heydari, M. Khansanami, V. Vatanpour and S. A. Mousavi, *Sep. Purif. Technol.*, 2022, **285**, 120291.
39 T. D. Kusworo, A. C. Kumoro, N. Aryanti, D. P. Utomo, H. Hasbullah, F. F. Lingga, A. Widiastuti, M. Yulfarida, F. Dalanta and T. A. Kurniawan, *J. Membr. Sci.*, 2022, **657**, 120663.
40 T. D. Kusworo, M. B. Puspa, A. C. Kumoro, M. I. Hanif, M. H. D. Othman, T. A. Kurniawan and D. P. Utomo, *J. Water Process Eng.*, 2025, **72**, 107415.

41 J. Pan, D. Hua, Y. Hong, X. Cheng, F. Guo, K. Bing Tan, Z. Zhong and G. Zhan, *Chem. Eng. J.*, 2023, **466**, 143164.
42 N. Sun, Z. Ren, P. Chen, M. Yue, J. Wu, Y. Fu and J. Ma, *npj Clean Water*, 2025, **8**, 19.
43 C. Esen, M. Antonietti and B. Kumru, *J. Appl. Polym. Sci.*, 2021, **138**, 50879.
44 C. Hu, Y.-R. Lin and H.-C. Yang, *ChemSusChem*, 2019, **12**, 1794–1806.
45 T. Meijer, H. Bazyar and B. Kumru, *ACS Appl. Eng. Mater.*, 2024, **2**, 2722–2732.
46 B. Kumru, D. Cruz, T. Heil and M. Antonietti, *Chem. Mater.*, 2020, **32**, 9435–9443.
47 C. Esen, M. Antonietti and B. Kumru, *ChemPhotoChem*, 2021, **5**, 857–862.
48 J. Han, H. Y. Zou, M. X. Gao and C. Z. Huang, *Talanta*, 2016, **148**, 279–284.
49 A. Charfi, H. Jang and J. Kim, *Bioresour. Technol.*, 2017, **240**, 106–114.
50 K. Cao, Z. Jiang, X. Zhang, Y. Zhang, J. Zhao, R. Xing, S. Yang, C. Gao and F. Pan, *J. Membr. Sci.*, 2015, **490**, 72–83.
51 K.-Y. Law, *Acc. Mater. Res.*, 2022, **3**, 1–7.
52 H. Darcy, *Les Fontaines Publiques de la Ville de Dijon*, Victor Dalmont, Paris, Paris, 1856.
53 G.-Q. Zhao, J. Zou, J. Hu, X. Long and F.-P. Jiao, *Sep. Purif. Technol.*, 2021, **279**, 119769.
54 A. M. Atta, A. O. Ezzat, S. A. Al-Hussain, H. A. Al-Lohedan, A. M. Tawfeek and A. I. Hashem, *React. Funct. Polym.*, 2018, **131**, 420–429.
55 L. Chi, Y. Qian, J. Guo, X. Wang, H. Arandiyan and Z. Jiang, *Catal. Today*, 2019, **335**, 527–537.
56 J. He, H. Sun, S. Indrawirawan, X. Duan, M. O. Tade and S. Wang, *J. Colloid Interface Sci.*, 2015, **456**, 15–21.
57 M. Tanzifi, M. Jahanshahi, M. Peyravi and S. Khalili, *J. Water Environ. Nanotechnol.*, 2023, **8**, 215–228.
58 S. Shi, M. Jia, M. Li, S. Zhou, Y. Zhao, J. Zhong, D. Dai and J. Qiu, *Colloids Surf., A*, 2023, **667**, 131259.
59 Z. Vilamova, P. Czernek, J. Zagora, L. Svoboda, J. Bednar, Z. Simonova, D. Placha and R. Dvorsky, *Appl. Surf. Sci.*, 2024, **677**, 161055.
60 L. P. Hastuti, A. H. Budiman, N. Darsono, G. E. Timuda, A. Bakri, A. Darmawan and O. P. Arjasa, *Fullerenes, Nanotubes Carbon Nanostruct.*, 2025, 1–14.
61 H. Lan, F. Wang, M. Lan, X. An, H. Liu and J. Qu, *Environ. Sci. Technol.*, 2019, **53**, 6981–6988.
62 J. Ran, T. Pan, Y. Wu, C. Chu, P. Cui, P. Zhang, X. Ai, C.-F. Fu, Z. Yang and T. Xu, *Angew. Chem., Int. Ed.*, 2019, **58**, 16463–16468.
63 Y.-J. Liu, *Water Sci. Technol.*, 2023, **88**, 169–184.
64 F. Dai, K. Xu, Z. Ke, M. Wang, C. Chen, G. Qian and Y. Yu, *Sep. Purif. Technol.*, 2023, **325**, 124708.
65 M. P. Wylie, S. E. J. Bell, P. Nockemann, R. Bell and C. P. McCoy, *ACS Omega*, 2020, **5**, 7771–7781.
66 H. Zhao, S. Ren, I. Zucker, Y. Bai and Y. Wang, *ACS ES&T Eng.*, 2022, **2**, 1239–1249.
67 X. Ye, R. Zhang, J. Zhou, S. Qiu and Y. Wang, *Langmuir*, 2025, **41**, 945–954.
68 M. Cifuentes-Cabezas, J. L. Bohórquez-Zurita, S. Gil-Herrero, M. C. Vincent-Vela, J. A. Mendoza-Roca and S. Álvarez Blanco, *Food Bioprocess Technol.*, 2023, **16**, 2126–2146.
69 Y.-J. Liu, *Water Environ. Res.*, 2022, **94**, e10748.
70 G. L. D. Pereira, L. Cardozo-Filho, V. Jegatheesan and R. Guirardello, *Membranes*, 2023, **13**, 290.